THE ASTRONOMICAL JOURNAL VOLUME 103, NUMBER 6 JUNE 1992

HOLMBERG II: A LABORATORY FOR STUDYING THE VIOLENT INTERSTELLAR MEDIUM

DANIEL PUCHE,[1,2] DAVID WESTPFAHL,[2] AND ELIAS BRINKS[1]

National Radio Astronomy Observatory, P.O. Box 0, Socorro, New Mexico 87801

JEAN-RENE ROY[3]

Département de Physique, and Observatoire du mont Mégantic, Université Laval, Québec G1K 7P4, Canada

Received 11 December 1991; revised 24 February 1992

ABSTRACT

VLA H I observations of Holmberg II (HoII=UGC 4305=DDO 50) at high spatial and velocity resolution show a stunning amount of detail in the form of H I shells and holes in its interstellar medium, similar to features seen in the Galaxy, M31 and M33. These features range in size from 100 to 1700 pc and show expansion velocities of typically 7 km s^{-1}. Their indicative ages range from 1 $\times$ 10^7 to 1.5 $\times$ 10^8 yr. There is a striking correlation between Hα emission, as seen in high quality CFHT CCD frames, and H I shells. The smaller holes tend to be filled with Hα emission whereas for the larger H I holes the Hα seems to be restricted to the edges. The most likely explanation for these features is in terms of events of sequential star formation whereby the combined effects of photoionisation, stellar winds, and supernovae of the most massive stars shape the interstellar medium. Some H II regions along the edges of larger shells may correspond to secondary sites of star formation. Massive stars, possibly in clusters, at the centers of the largest holes provide supporting evidence for the above picture. Infall of material, although not ruled out, is not needed to explain the overall features or large dimensions of the holes. The H I holes in HoII are much larger than those found in more massive spiral galaxies. This is attributed to HoII having an H I scale height of h=625 pc rather than the more usual 120 pc. The scale height is derived independently by measuring the velocity dispersion of the gas which is of order 6–7 km s^{-1} and combining it with a mass model which is derived on the basis of the H I rotation curve. This larger scale height translates to a lower gas volume density which facilitates the expansion of H I shells. In addition they can expand to larger dimensions before experiencing blow-out. The global H I distribution is typical of a late-type gas rich dwarf system. The velocity field shows a rapid rise of the rotation velocity in the inner parts and a flat rotation curve in the outer regions out to a radius of 7.5 kpc. At large radii HoII displays a symmetrical warp. A total H I mass of $\mathcal{M}_{\rm H\,I}$ = 7 $\times$ 10^8 $\mathcal{M}_\odot$ and a total kinematical mass of $\mathcal{M}_{\rm total}$ = 2 $\times$ 10^9 $\mathcal{M}_\odot$ are derived, indicating that HoII has a large fraction of its mass in the form of gas, about 50% when corrected for the contribution of He. The flatness of the rotation curve at the last measured point implies the presence of dark matter. In a few areas, mostly near H II regions, we find peak H I brightness temperatures as high as 150–250 K, a much higher value than in the Galaxy. The reason for the observed brightness temperatures is not well understood. It could be due to a different energy balance in the ISM of HoII which is linked to a lower heavy element abundance, preventing efficient cooling, and a strong interstellar radiation field. A simpler explanation is that a large fraction of the neutral gas is in the warm phase such that line-of-sight integration produces the observed peak brightnesses.

1. INTRODUCTION

Sites of recent massive star formation, in the Galaxy and other nearby spirals, show the effects of stellar winds and supernova shocks on the surrounding interstellar medium (ISM). Observations of the Galaxy by Heiles (1979, 1984; for a review on the state of the ISM of the Galaxy see, e.g., Kulkarni & Heiles 1987, 1988) have revealed the presence of large coherent structures in the ISM such as H I shells and bubbles. Although hard evidence regarding the origin of these structures is difficult to come by because of our location within the disk of the Galaxy, circumstantial evidence suggests that the combined effects of stellar winds and multiple supernova explosions (SNe) are the most likely mechanism for producing these features (Cash *et al.* 1980). Observations in the early eighties of our nearest neighbors using spectral line synthesis imaging with the Westerbork Synthesis Radio Telescope (WSRT) revealed

[1]The National Radio Astronomy Observatory is operated by Associated Universities, Inc., under cooperative agreement with the National Science Foundation.

[2]Visiting Astronomer, Kitt Peak National Observatory and Warner and Swasey Observatory of Case-Western Reserve University, National Optical Observatories, Operated by AURA, Inc., under contract with the National Science Foundation.

[3]Visiting Astronomer, Canada–France–Hawaii Telescope operated by the National Research Council of Canada, the Centre National de la Recherche Scientifique de France and the University of Hawaii.

 0004-6256/92/061841-18$00.90

similar structures in M31 (Brinks, 1981; Brinks & Bajaja 1986, hereafter referred to as BB86) and M33 (Deul & den Hartog 1990), confirming the earlier notions regarding the origin and evolution of H I shells and bubbles in the ISM (for a review on studies of the cool atomic component of the ISM in nearby galaxies see, e.g., Brinks 1990).

The large scale structures which are now so apparent were predicted by Cox & Smith (1974). They recognized that the hot gas which is produced in a supernova explosion is long lived (say 5×10^6–5×10^8 yr depending on temperature) and that at the expected supernova rate of a few per century, the ISM should be dominated by blown cavities. This picture was a substantial modification of the Field *et al.* (1969) two-phase medium. It implied that the ISM has three distinct phases, a cool ($T \sim 100$ K), a warm ($T \sim 10^4$ K), and a hot phase ($T \sim 10^6$ K). Various refinements have been proposed, but this picture basically still stands (see Norman & Ikeuchi 1989; for a review of the theoretical aspects see, e.g., Tenorio-Tagle & Bodenheimer 1988, hereafter referred to as TTB88). Although the importance of SNe and of their impact on the ISM remains unchallenged, some questions have been raised regarding the creation of the largest holes. The energetics required to create the supershells can be of the order of 10^{54} ergs, or equivalent to the kinetic energy output of $\sim 10^3$ SNe. An alternative explanation was put forward by Tenorio-Tagle *et al.* (1987) who favor impacts of small, high-velocity clouds. This model is suggested by H I observations of M101 published by van der Hulst & Sancisi (1988).

Our project aims at understanding the creation and evolution of H I shells and bubbles in the ISM of disk systems. Intimately linked to this is the question of what drives star formation. To study systems which should be simpler, at least in principle, than spiral galaxies, we have turned to dwarf galaxies. They lack a clear spiral pattern and the accompanying density wave which, in bigger spirals, drives star formation. Because dwarf galaxies exhibit low rotational velocities and generally solid-body rotation curves, features in their ISM tend to be longer lived than in spirals. They also tend to have low abundances of heavy elements which may be an important factor regulating star formation. Due to their small linear size and mass, their probability to suffer impacts from clouds or cloudlets is smaller than for large galaxies.

With the NRAO VLA in B array, angular resolutions of 5″ can be achieved at velocity resolutions of 2.5–10 km s^{-1}. The H I structures we are interested in have linear sizes ranging from 50–1000 parsec. To resolve these features, we are restricted to objects less distant than 5 Mpc. This led us to observe the dwarf companions to M81, which lies at a mean distance of 3.2 Mpc (de Vaucouleurs 1978; Aaronson & Mould 1983; Bottinelli *et al.* 1984; Humphreys *et al.* 1986; Freedman & Madore 1988; Jacoby *et al.* 1989, but see Sandage 1984). We selected Holmberg II as our first target, based on its high gas content, favorable inclination and on the fact that studies at other wavelengths were available. The VLA H I observations of this galaxy show a stunning amount of structure in the form of H I shells and holes. Many of the H I structures have counterparts in Hα images linking the origin of these features to the formation and later death of massive stars.

TABLE 1. Optical data on HoII.

Morphological type	Im IV-V
α (1950)	$8^h14^m6^s$
δ (1950)	+70°52′
Isophotal major diameter, D_{25}	8.2′
Axis ratio, $q=b/a$	0.74
Inclination, i	47°
Corrected total B magnitude, $B_T^{0,i}$	10.92
Adopted distance (Mpc)	3.2 (1′=0.93 kpc)
Absolute B magnitude, $M_B^{0,i}$	−16.61
Total blue luminosity ($\mathcal{M}_\odot = 5.43$), $L_{B\odot}$	0.67×10^9

HoII has previously been observed at 21 cm by many authors including Rots (1980), Thuan & Martin (1981), Davis & Seaquist (1983), and most recently Huchtmeier & Richter (1986, 1988). Coltrell (1976) used the Cambridge Half-Mile telescope to map HoII in the line of H I with an angular resolution of 2′. Table 1 summarizes some pertinent data mostly taken from Huchtmeier & Richter (1988).

2. 21 cm OBSERVATIONS AND DATA REDUCTION

The H I emission of HoII was observed with the VLA using three configurations, B, C, and D (the parameters of the observations are given in Table 2). We spent 7 hr in the B configuration, 5 hr in C, and 2 hr in D. The longer observing time in the B array was necessary to compensate for the lower surface brightness sensitivity in this extended configuration. We selected a 1.56 MHz bandwidth centered at a heliocentric radial velocity of 190 km s^{-1}, placing the H I emission from the Milky Way just outside the low-velocity edge of our band. The band was divided in 128 channels resulting in a velocity resolution of 2.58 km s^{-1} after application of on-line Hanning smoothing. The absolute flux calibration was determined by observing 3C 286 for approximately 10 min in each configuration, assuming a flux density of 14.86 Jy according to the Baars *et al.* (1977) scale. This calibrator was also used to derive the complex bandpass corrections. The nearby calibrators 0859

TABLE 2. Parameters of the VLA observations.

Dates of observations	B array 1990 August 10 C array 1990 December 2 D array 1991 March 6
Primary beam at half-power (FWHM)	~32′
FWHM of synthesized beam (full resolution)	4.0″×4.5″
Total bandwidth	1.56 MHz
Central velocity, heliocentric	190 km s^{-1}
Channel width	2.58 km s^{-1}
rms noise in channel maps (full resolution)	1.54 mJy beam^{-1}
Conversion factor, equivalent of 1 mJy beam^{-1}	
4.0″×4.5″	33 K
11.0″×10.9″	5 K
27.9″×27.3″	0.8 K

+681 and 0836+710 were used as secondary amplitude and phase calibrators. The calibration of the individual databases was performed using the standard procedures in the NRAO package AIPS. The *uv* data were inspected and edited to remove bad data points due to either interference or crosstalk between antennae, after which the data were calibrated. All the *uv* data were combined into a single database which was subsequently used for the mapping.

The field of HoII contains little radio continuum emission, most of it coming from an unresolved background point source northeast of the galaxy. No emission from HoII was evident in a continuum map based on line-free channels, due to our modest total bandwidth of 1.56 MHz. The 20 cm radio continuum was previously studied by Condon (1987), who used the VLA in the D array and showed that continuum emission comes from two distinct regions in the disk of HoII, centered on the most active star-formation regions. The total observed continuum flux density is 22.1 mJy, corresponding to a luminosity of 3.2×10^{19} W Hz^{-1}. Because of the high local rate of star formation in the system, this emission is suspected to be mainly of thermal origin. Condon's resolution was not sufficient to do an accurate comparative study of the radio continuum and the star-forming regions. Observing time for a more sensitive, higher resolution, multifrequency radio continuum study with the VLA is needed.

The continuum emission was subtracted in the *uv* data with the AIPS task UVBAS (van Langevelde & Cotton 1990) using channels which were free of line emission. Three sets of maps were then produced, one with uniform weighting and no taper, one with natural weighting and no taper, and one with uniform weighting and a $5 \times 5k\lambda$ (kilo wavelength) taper in u and v. These maps, labeled high, medium, and low resolution, have spatial resolutions of respectively $4.0'' \times 4.5''$, $11.0'' \times 10.9''$, and $27.9'' \times 27.3''$, corresponding to 60, 170, and 420 pc at the distance of HoII. The naturally weighted and the tapered maps were CLEANed down to approximately the 1σ noise level of a line-free map. The uniformly weighted, untapered, maps did not need to be cleaned because the spectral signal in individual channel maps was not strong enough to produce significant sidelobes.

The high resolution channel maps are shown in Fig. 1 [Plates 103–106]. Every other channel over the frequency range where there was signal is shown. The heliocentric radial velocities (to the nearest integer) are indicated in the upper left-hand corner of each plane. The most striking feature in these maps is the obvious presence of large empty regions surrounded by H I emission in several velocity channels. These holes will be the main topic of this paper. Another important feature of these images is the pronounced symmetrical warp of the outer H I disk. As will be shown in the next section, the rotational parameters from the low resolution data show a smooth variation of position angle (P.A.) as a function of radius.

3. H I DISTRIBUTION AND VELOCITY FIELD ANALYSIS

The global H I profile of HoII, obtained by summing the total amount of H I in each channel map of the naturally weighted datacube (corrected for primary beam attenuation), is shown in Fig. 2. The midpoint velocity derived from this profile is 158 ± 2 km s^{-1}, and the velocity widths are $\Delta V_{20} = 71$ km s^{-1} and $\Delta V_{60} = 55$ km s^{-1}. This is in excellent agreement with the value of 158 ± 5 km s^{-1} for the systemic velocity and $\Delta V_{20} = 73$ km s^{-1} as given by Tully (1988). Integrating over the H I line profile we find a total H I flux of 327 Jy km s^{-1} compared to a value of 360 Jy km s^{-1} given by Huchtmeier & Richter (1986). This means that despite the large extent of the emission which is evident in the channel maps, our interferometer data recover at least 90% of the H I emission in HoII. Structures larger than 15′ are not seen by our VLA configurations. This is confirmed when deriving the global profile using the uniformly weighted (tapered or not) cube, which gives us only 50% of the total flux. This is due to the fact that a lot of H I is in extended structures to which the uniformly weighted data is less sensitive. The total H I mass derived from the integrated flux in our naturally weighted cube is $\mathcal{M}_{\rm H\,I} = 7 \times 10^8\, \mathcal{M}_\odot$.

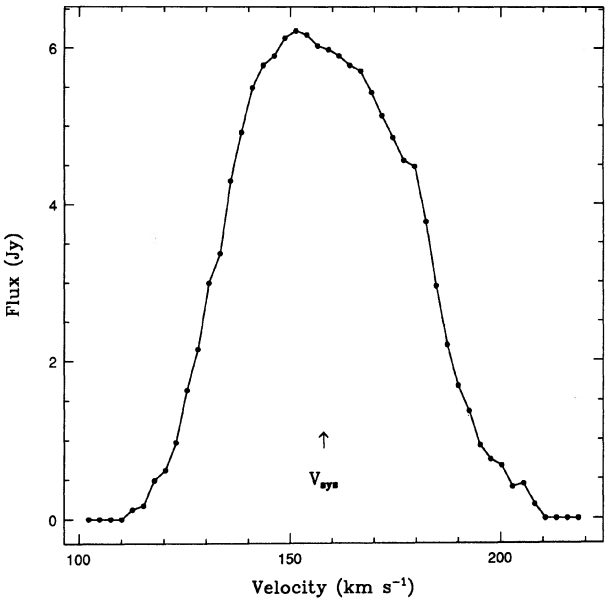

FIG. 2. Global H I profile for Holmberg II obtained by integrating the channel maps over the area of the source after subtraction of the continuum background and corrected for the primary beam attenuation. The channel spacing is 2.6 km s^{-1}. The arrow labeled V_{sys} indicates the systemic velocity of 158 km s^{-1}.

The high resolution data cube was used to produce moment maps of the H I distribution. Figure 3 [Plate 107] shows the total H I distributions of the high resolution and medium resolution data, obtained by summing velocity channels while applying a Gaussian smoothing of a factor of 2 in the maps and a 3 channel spectral Hanning smoothing. The H I reaches out to about $1.5D_{\rm Ho}$ (the Holmberg diameter is defined by the B isophote at 26.6 mag arcsec^{-2}). The distribution is quite chaotic and the presence of holes is obvious in this image. A large H I cloud is visible to the southwest of the galaxy in the medium resolution image. It extends to twice the size visible

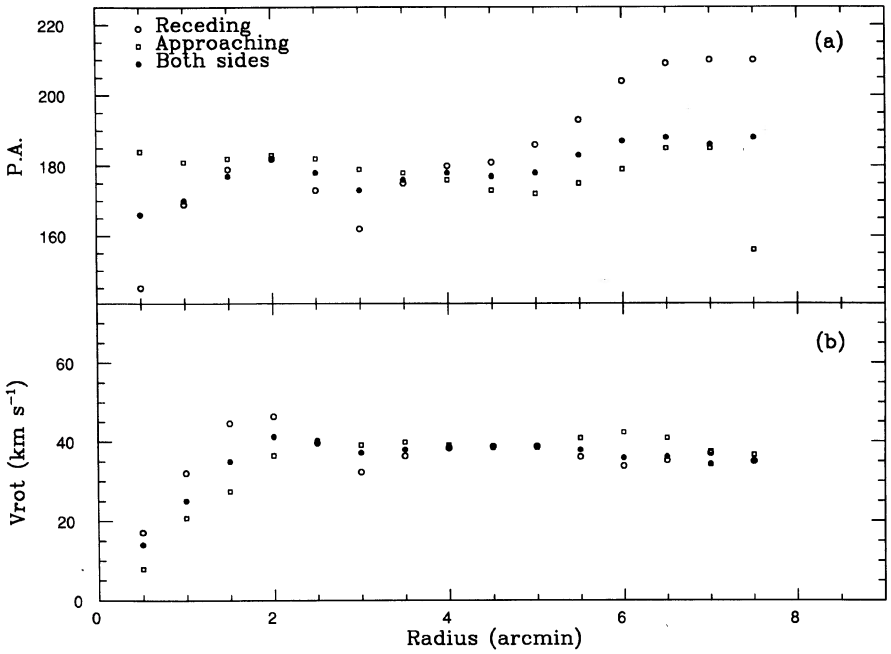

FIG. 5. Least-squares solution for (a) P.A., and (b) V_{rot} derived from the velocity field at 45″ resolution. A global solution (filled circles) and separate solutions for the approaching and receding sides are shown.

in Fig. 3. The corresponding velocity fields (Fig. 4 [Plate 108]) show the presence of a significant warping of the disk, which can be identified as a change of position angle of the isovelocity contours as a function of galactocentric radius.

The medium resolution velocity field and an additional very low resolution velocity field, obtained from a moment analysis of a datacube of 45″ resolution to reveal the faintest structures, were used to derive a rotation curve for HoII. To obtain the rotation curve a set of orientation parameters [rotation center (x_0,y_0), systemic velocity V_{sys}, inclination i, position angle P.A.] that best represent the observed velocity field at all radii must be found. The method used is described by Begeman (1989) and van Albada *et al.* (1985). The dynamical center and the systemic velocity are determined jointly, using only the inner regions of the velocity field while keeping i and P.A. fixed (using the optical values as a first guess). The data in an opening angle of 100° about the minor axis are excluded from the analysis to minimize the errors due to deprojection effects. We find that the rotation center corresponds, within the resolution of the H I data, to the optical center [$\alpha(1950.0) = 08^h14^m06^s$, $\delta(1950.0) = 70°52'00''$], and that $V_{sys} = 156.8 \pm 3$ km s^{-1}, in agreement with the global profile.

The next step is to obtain a least-squares solution for i, P.A., and V_{rot} in concentric annuli in the plane of the galaxy. Even though the highly smoothed data were used, it proved to be difficult to keep the inclination from varying from one ring to the next because of the irregular distribution of H I and deviations from smooth flow in the velocity field due to the expanding shells. The one sigma amplitude of the variations was ~5°. Since no systematic trends were seen in the variation of the inclination as a function of radius, the average value of $i = 40° \pm 5°$ was kept fixed in the final analysis. As a test of the parameters, separate solutions were obtained for the approaching and receding sides and are presented in Fig. 5. The position angle varies systematically from the inner to the outer regions on both sides of the galaxy with a total range of ~41°, the mean position angle is P.A. = 177°. The receding side of the rotation curve has a more rapid rise than the approaching side but in the outer parts both sides exhibit a slight decline of the rotation velocity. These anomalies could be real or could be due to the uncertainty in the inclination of the galaxy as a function of radius.

The rotation curve was derived independently for the medium and low resolution datasets and gives similar results, given that the medium resolution curve is noisier. The innermost regions could not be studied by the medium resolution dataset because of insufficient uniformity in the gas distribution, so we decided to restrict ourselves to the results from the low resolution data. Our adopted rotation curve is given in Table 3 and shown in Fig. 6. The errors correspond to one-half of the largest difference between the rotation curve found for the whole galaxy and the rotation curves derived for each side. This is a more realistic estimate of the uncertainties on V_{rot} than the much smaller formal errors given by the least-squares analysis.

Once the orientation parameters of HoII were found, we derived the elliptically averaged profile of the H I gas shown in Fig. 7 and listed in Table 4 in units of atoms cm^{-2} corrected for the inclination of the galaxy. It was obtained by averaging the surface densities in rings on

TABLE 3. Adopted rotation curve for HoII.

Radius (arcmin)	V_{rot} (km s^{-1})	Error (km s^{-1})
0.5	13.98	±3.03
1.0	25.00	±3.54
1.5	34.97	±4.85
2.0	41.25	±2.56
2.5	40.27	±0.30
3.0	37.18	±2.43
3.5	37.98	±0.80
4.0	38.70	±0.21
4.5	38.45	±0.18
5.0	38.50	±0.15
5.5	37.89	±1.49
6.0	35.84	±3.23
6.5	36.12	±2.40
7.0	34.26	±1.59
7.5	35.00	±0.82

the medium resolution, naturally weighted total H I map. The surface density is uneven in the central region out to $r \simeq 3'$. This is due to the presence of the holes which influence the sum over small rings. The density then drops smoothly out to a radius of $\sim 8'$. The last column of this table is the volume density of the gas assuming a disk scale height of 625 pc. The total path through the Gaussian distribution is taken to be $h\sqrt{2\pi}$. The derivation of the scale height is discussed in Sec. *8.2*.

4. Hα DISTRIBUTION AND BROAD-BAND SURFACE PHOTOMETRY

The Hα images of the central parts of Holmberg II were acquired on 1990 March 12 at the Cassegrain focus of the 3.6 m Canada–France–Hawaii Telescope on Mauna Kea with the PALILA focal reducer which reimages the telescope's $f/8$ focal plane on a CCD at $f/2$. The detector was

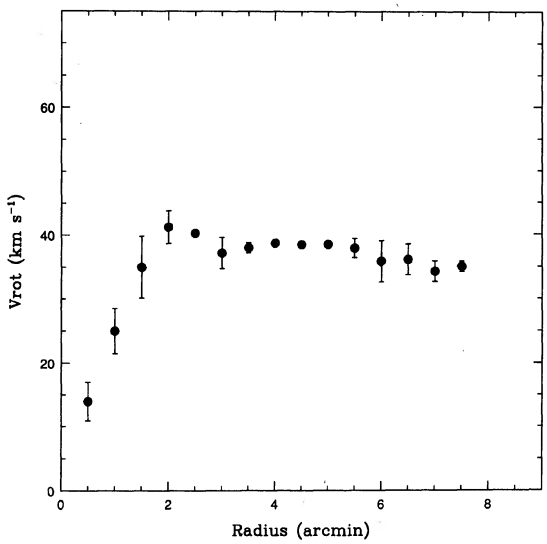

FIG. 6. Adopted H I rotation curve for Holmberg II. The error bars are one half of the largest difference between the solution for both sides and either the approaching or the receding side.

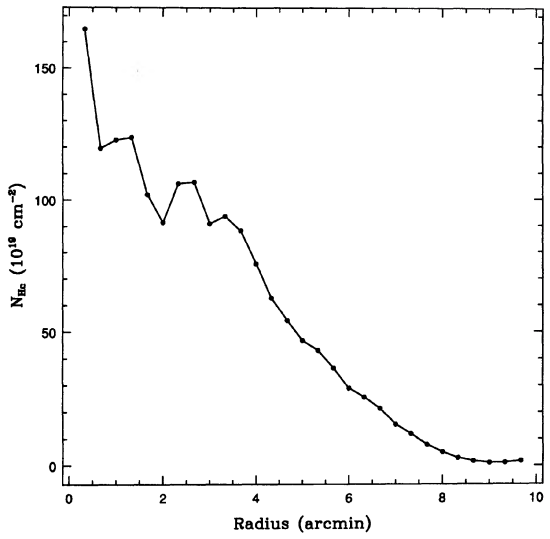

FIG. 7. H I radial distribution obtained by averaging the surface densities of the 11.0″×10.9″ total H I map in circular annuli in the plane of the galaxy. The parameters used for the deprojection are P.A.=177° and i=41°.

PHX1, a Ford Aerospace front-side illuminated CCD with 20 μm square pixels in a 512×512 format, the readout noise was 7.1 electrons rms. The pixels subtended 0″.57 on the sky, yielding a total field of view of ~5×5 arcmin. The seeing varied between 0″.7 and 0″.8 during the exposures,

TABLE 4. H I radial distribution of HoII.

Radius (′)	n_{Hc} (10^{19} cm^{-2})	n_{Hc} ($\mathcal{M}_\odot$ pc^{-2})	$n_{H\,I}$ (cm^{-3})
0.33	165.0	13.2	0.34
0.67	119.5	9.6	0.25
1.00	122.7	9.8	0.26
1.33	123.6	9.9	0.26
1.67	102.0	8.2	0.21
2.00	91.5	7.3	0.19
2.33	106.2	8.5	0.22
2.67	106.8	8.5	0.22
3.00	91.0	7.3	0.19
3.33	93.8	7.5	0.19
3.67	88.3	7.1	0.18
4.00	75.6	6.0	0.16
4.33	62.7	5.0	0.13
4.67	54.2	4.3	0.11
5.00	46.8	3.7	0.10
5.33	43.0	3.4	0.09
5.67	36.5	2.9	0.07
6.00	29.0	2.3	0.06
6.33	25.6	2.0	0.06
6.67	21.4	1.7	0.05
7.00	15.4	1.2	0.03
7.33	12.0	1.0	0.02
7.67	7.8	0.6	0.02
8.00	5.1	0.4	0.01
8.33	2.9	0.2	0.01
8.66	1.7	0.1	0.004
9.00	1.1	0.1	0.002
9.33	1.1	0.1	0.002
9.67	1.8	0.1	0.004

indicating that we were undersampling the actual image profile of point sources. Images were obtained through a narrow-bandwidth Hα filter (λ=6570 Å, $\Delta\lambda$=10 Å), a filter at λ6605 Å ($\Delta\lambda$=10 Å) was used to derive the contribution of the red continuum. Total exposure time was 3000 s at Hα and 900 s in the continuum. The galaxy is much fainter in the continuum than in the line; thus the final continuum-subtracted Hα image was not affected by the noise introduced by the short exposure in the continuum. We followed the procedures of Martin *et al.* (1989) and Belley & Roy (1992) for image reduction. The resulting Hα image is shown in Fig. 8 [Plate 109]. The image covers an area of approximately 5′×5′ centered at $\alpha(1950) \simeq 8^h14'$, $\delta(1950) \simeq 70°52'$, and corresponds only to a fraction of the field sampled in H I.

Obviously, there is a large amount of structure in this image, the main feature being an overall distribution of bright H II regions in a large circular pattern. The boxed region encloses one giant H II region which was measured by Kennicutt (1978) and which we used for calibrating our image.

A second set of optical images was obtained during an observing run at Kitt Peak National Observatory on 1991 May 16–20 with the Burrell Schmidt Telescope of Case-Western Reserve University. This run was used to make Hα images of the entire field of the H I data. The ST2K CCD with 21 μm pixels, each covering about 2″ on the sky and giving a field of more than one degree, was used to search for extended emission in and around the galaxy. Filters centered at λ6563 Å and λ6477 Å ($\Delta\lambda$=75 Å) from Kitt Peak Hα filter set B were used for the on and off-band images, respectively. For each filter all images were registered using several stars in close proximity to the galaxy and combined using a min-max sigma clipping task within IRAF to eliminate cosmic ray events and cosmetic defects. Several stars in regions with no obvious Hα emission were used to scale the on- and off-band images for continuum subtraction. The H I structures will be compared to this Hα image in Sec. 7.

During the same observing run a series of *R* band images was taken to compare the smooth distribution of stars with the H I holes and Hα shells. Three exposures of 1200 s and three of 300 s were made to assure detection of the faint outer galaxy and avoid saturation of the brighter inner galaxy. The telescope was moved several pixels between exposures so that the median of all frames of a given exposure time could be taken to eliminate image defects. The image was left uncalibrated, so this should be viewed as a detection experiment only. The final image will be discussed in more detail in Sec. 7.

5. CATALOG OF H I HOLES

In the absence of a reliable unbiased search algorithm for recognizing holes in the H I distribution, one must rely on visual inspection. In the case of M31, strong emission was visible in individual channel maps and because of its large inclination angle several velocity profiles were often seen in one line of sight. In the case of HoII both the lower surface brightness in individual channels and the lower inclination make a search in the total H I map far more reliable and complete.

Both the high and medium resolution maps were used to search for candidate holes on the NRAO IIS image display system using criteria (iii), and (iv) from BB86: a strong density contrast with respect to the surrounding emission, and a shape definable by an ellipse. To reduce personal bias, independent lists of candidates were compiled by three of us (D.P., D.W., and E.B.). The lists of candidates were then compared and the differences discussed in detail. It turned out that all of the differences originated from applying different criteria when separating partially complete rings into multiply connected holes. The lists differed by no more than 10% in the number of holes identified by DP and EB, while DW identified all the large structures without separating them into multiple holes. After reexamining the debated structures we came to a common final list of 51 holes. This list might still suffer from personal biasing by the authors but at an insignificant level for the discussion which follows. The centroid position of the holes as well as the coordinates of the major and minor diameters were obtained by placing a crosshair on the structures and recording the positions in relative coordinates in the images. The coordinates derived by all of the authors did not differ by more than a few picture elements and are accurate to approximately 0.1′.

With the final list of candidate holes in hand, a systematic analysis of the velocity profiles was made. Because of the low brightness contrast between the shells and the face of the holes, it turned out to be very difficult to look for expansion in position-velocity cuts (*L-V* diagrams) through the holes as was done on M31 by BB86. Moreover, the fact that HoII is at 3 Mpc compared to 700 pc for M31 also means that we were sensitivity limited on the faces of the expanding shells, hence worsening the problem of identifying the front and back. Some of the holes were difficult to identify as such in the *L-V* diagrams because of lack of sensitivity or, more importantly, because of confusion due to crowding of the holes. We flag these in Table 5 with a question mark added to the value of the expansion velocity. An *L-V* diagram at the velocity and latitude of hole number 35 is shown in Fig. 9. This is one of the best examples of a completely enclosed hole and it can be seen that unambiguously defining the edge is difficult. A better way to clearly measure the expansion velocities was to plot a series of spectra through the holes and then fit the components with variable width Gaussians. This analysis was performed by using the one dimensional spectroscopic analysis facilities in the NOAO package IRAF. We plotted spectra at each pixel in the low resolution datacube in a preliminary search for double peaked profiles. Each hole had on average half a dozen double peaked spectra which could be fitted by two Gaussians. The widths and the separations of the peaks were measured by making a fit to the observed lines. For each hole the expansion velocity is given by half the separation between the peaks. We corrected the expansion velocities for the pixels which were not centered on the holes by applying a cosine correction as

TABLE 5. Observed properties of H I holes.

No.	X (′)	Y (′)	α (1950)	δ (1950)	DV (km s^{-1})	MAJ (pc)	MIN (pc)	P.A. (°)
1	5.0W	0.1N	08 13 05	70 52 07	4.1	716	480	5
2	4.6W	1.9N	08 13 11	70 53 52	4.8	1275	857	155
3	4.4W	1.0N	08 13 12	70 53 01	3.0	1128	409	106
4	4.4W	4.5N	08 13 13	70 56 30	4.1	989	888	158
5	4.1W	0.7S	08 13 16	70 51 18	8.9	1297	1060	43
6	3.5W	2.3S	08 13 24	70 49 44	1.0	183	96	112
7	3.4W	2.1N	08 13 25	70 54 06	4.7	341	305	6
8	3.3W	3.8N	08 13 26	70 55 48	5.5	1561	1463	0
9	3.2W	3.0N	08 13 28	70 55 00	4.9	1158	713	5
10	3.0W	1.3S	08 13 30	70 50 42	8.8	1205	1009	122
11	2.8W	4.9N	08 13 32	70 56 55	5.0?	543	441	0
12	2.4W	0.9N	08 13 37	70 52 54	7.7	420	258	76
13	1.9W	4.1S	08 13 43	70 47 54	7.0	1897	1130	43
14	1.9W	0.8N	08 13 44	70 52 49	3.9	413	379	99
15	1.8W	5.4N	08 13 45	70 57 25	2.0?	557	336	38
16	1.6W	0.2N	08 13 47	70 53 13	1.0	206	170	9
17	1.6W	2.9N	08 13 47	70 54 54	2.7?	848	646	90
18	1.6W	3.4N	08 13 47	70 55 22	2.5?	510	509	176
19	1.5W	2.3N	08 13 48	70 54 19	3.0?	648	527	43
20	1.4W	0.1N	08 13 49	70 52 06	6.5?	136	102	0
21	1.2W	1.4S	08 13 52	70 50 38	6.6	1765	1663	0
22	1.0W	0.5N	08 13 54	70 52 31	6.5	577	396	118
23	1.0W	0.9N	08 13 54	70 52 52	4.5	781	435	56
24	0.8W	1.4N	08 13 56	70 53 25	7.5?	170	136	90
25	0.8W	3.2N	08 13 57	70 55 13	3.4	714	615	3
26	0.6W	3.6N	08 13 59	70 55 36	3.1?	280	173	14
27	0.4W	4.5S	08 14 01	70 47 32	4.8	1156	744	40
28	0.4W	0.9N	08 14 01	70 52 54	7.2?	339	238	0
29	0.3W	0.3S	08 14 02	70 51 44	3.9	607	320	153
30	0.4W	1.7N	08 14 02	70 53 43	8.1	1052	987	90
31	0.3W	1.2N	08 14 03	70 53 12	2.5?	272	272	0
32	0.2W	0.8S	08 14 04	70 51 12	4.8	759	396	153
33	0.1W	2.3N	08 14 05	70 54 19	3.5	476	280	176
34	0.0	3.6N	08 14 06	70 55 36	5.7	514	442	82
35	0.0	4.2N	08 14 06	70 56 12	10.5	640	577	122
36	0.1E	0.6N	08 14 07	70 52 37	8.3	687	432	123
37	0.2E	2.7N	08 14 08	70 54 40	11.9	379	228	153
38	0.2E	5.4N	08 14 08	70 57 25	6.4	987	781	86
39	0.4E	2.1N	08 14 11	70 54 06	3.5	373	305	0
40	0.6E	2.0S	08 14 13	70 50 02	3.5?	204	136	0
41	0.6E	1.3S	08 14 13	70 50 41	6.2?	274	170	7
42	0.5E	2.6N	08 14 13	70 54 36	10.1	407	274	0
43	0.7E	0.5S	08 14 15	70 51 30	4.8	240	240	45
44	0.7E	0.9N	08 14 15	70 52 55	7.9	826	607	71
45	0.8E	2.7N	08 14 15	70 54 43	6.6	576	379	135
46	0.8E	1.7S	08 14 16	70 50 18	8.0?	304	170	27
47	1.2E	2.8S	08 14 20	70 49 14	6.2	1395	1256	131
48	1.5E	2.3N	08 14 24	70 54 18	14.1	838	653	122
49	1.5E	3.5N	08 14 24	70 55 30	6.9	1370	1188	132
50	2.2E	0.2N	08 14 33	70 52 13	13.9	775	653	23
51	2.3E	3.0N	08 14 33	70 55 01	6.2	1426	1252	142

a function of normalized distance (by the size of the hole) from the center. The justification for this correction is clear when one looks at the profiles and sees that the expansion velocities do indeed follow a centrosymmetrical pattern as is shown in Fig. 10 where we plot a few pixels in and around hole number 35. It is even more obvious when crosscuts, in lines of constant right ascension and declination, are used to derive the expansion velocity at every pixel across the face of the hole. Figure 11 gives the expansion velocities derived from using all the profiles on the

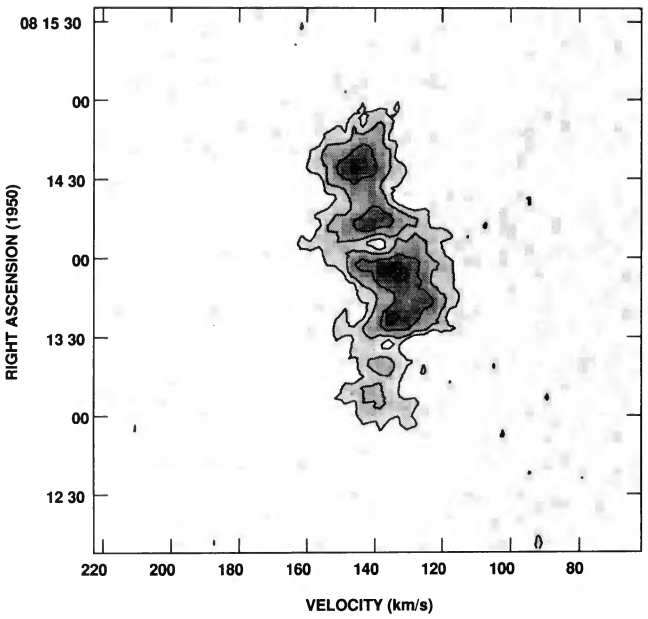

FIG. 9. Position-velocity diagram at the position and velocity of hole number 35 ($\alpha \simeq 8^h14^m$, $V \simeq 140$ km s^{-1})

medium resolution datacube in two perpendicular lines across hole number 35. The solid line represents a cosine function and shows that the expansion is spherical. This spherical expansion is evidence for a central origin of the holes, as opposed to a wall of star formation pushing the H I outwards as the winds evolve. This will be important in the discussion of Sec. 8.3.

We also used the H I profiles to derive the minimum velocity dispersion in the disk by looking at quiescent regions. Several lines of sight were averaged and gave a velocity dispersion of 6.8 ± 1.0 km s^{-1}. This shows that our velocity resolution of 2.5 km s^{-1} was barely adequate to resolve the lines of neutral hydrogen. An interesting effect is observed in the shells of the expanding bubbles. Gener-

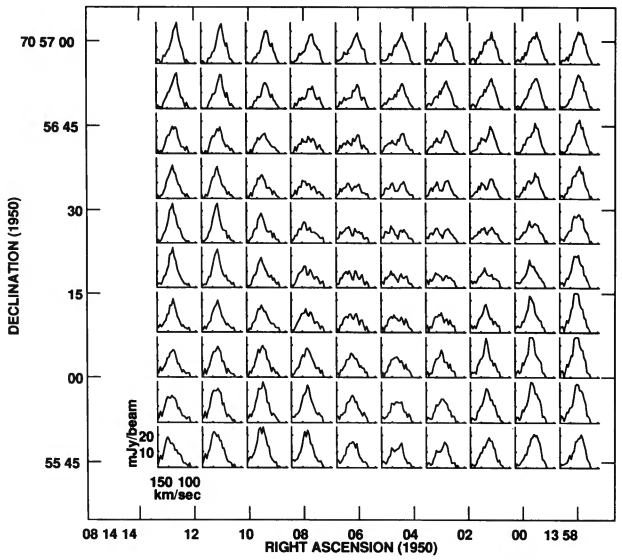

FIG. 10. H I velocity profiles in and around hole number 35 obtained from the 27.9″×27.3″ resolution datacube.

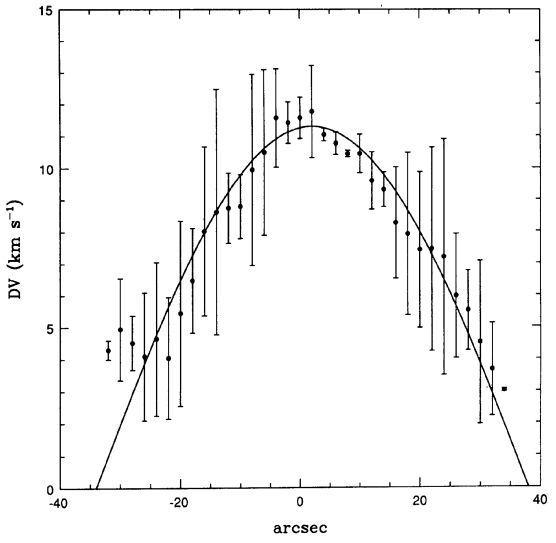

FIG. 11. Expansion velocities at 2″ intervals measured along two perpendicular lines passing through the center of hole number 35. The error bars represent the difference in measured expansion between the two orthogonal directions. The solid line is a cosine function indicating that the expansion is spherical.

ally the velocity dispersion in these structures is twice the value of quiescent regions. This could indicate that turbulent motions are induced by the triggering events which form the bubbles, or that the expansion velocities are showing the presence of clouds left behind the shock which are being sampled through the line of sight.

The catalog of the observed properties of H I holes is presented in Table 5. For purposes of comparison, this list follows as closely as possible the form used by BB86. For each hole, the properties listed are as follows:

Column 1: Number of the hole.

Columns 2 and 3: Position of the center of the hole in arcminutes in the direction of right ascension and declination relative to the pointing center of the H I observations which corresponds approximately to the center of the galaxy. The holes are ordered in order of increasing right ascension. The reference position is $\alpha(1950) = 8^h14^m6^s$, $\delta(1950) = 70°52'00''$. Note that in BB86 the coordinates are rotated in order to align X and Y with the major and minor axis of M31. The suffix N, E, S, and W to indicate the direction is preferred to the potentially ambiguous + and − signs.

Columns 4 and 5: Position of the center of the hole in α and δ (1950.0).

Column 6: Expansion velocity of the hole where it can be measured. The accuracy of DV is about 1.0 km s^{-1}.

Columns 7 and 8: Major and minor axis diameters measured in parsecs.

Column 9: Position angle of the major axis of the hole. The angle is measured in degrees counterclockwise (i.e., to the east) with respect to the north declination axis.

Table 6 lists additional properties derived from the H I observations.

Column 1: Number of the hole.

TABLE 6. Derived properties of H I holes.

No.	R (kpc)	Θ (°)	Diam. (pc)	Ratio	P.A. (°)	Age (10^6 yr)	Mass ($10^4 \mathcal{M}_\odot$)	Energy (10^{50} ergs)
1	6.65	92	586	0.67	5	70.9	5.2	2.5
2	6.40	108	1045	0.67	155	106.6	29.5	18.7
3	6.01	101	679	0.36	106	110.8	16.2	5.3
4	7.48	128	937	0.90	158	111.9	5.3	2.5
5	5.52	83	1173	0.82	43	64.1	125.1	210.5
6	5.10	64	132	0.53	112	64.8	0.2	0.02
7	5.05	116	323	0.90	6	33.6	3.6	2.1
8	5.92	131	1512	0.94	0	135.7	178.5	148.8
9	5.26	126	909	0.62	5	90.8	77.7	56.5
10	4.17	72	1103	0.84	122	61.3	208.1	370.0
11	6.36	143	489	0.81	0	47.9	3.0	1.9
12	3.30	107	329	0.62	76	20.9	9.9	13.2
13	4.83	31	1464	0.60	43	102.4	365.5	468.7
14	2.64	109	396	0.92	99	49.7	19.8	11.0
15	6.07	156	432	0.60	38	105.8	4.1	0.7
16	2.14	97	187	0.82	9	91.6	1.9	0.2
17	3.66	145	740	0.76	90	136.7	78.5	26.1
18	4.06	148	510	1.00	176	101.8	20.5	5.7
19	3.17	139	584	0.81	43	97.0	54.5	21.2
20	1.87	94	118	0.75	0	10.5	0.6	0.4
21	2.06	48	1713	0.94	0	127.1	1495.2	2025.0
22	1.49	112	478	0.69	118	35.7	31.0	35.0
23	1.65	123	583	0.56	56	64.1	59.1	41.1
24	1.85	143	152	0.80	90	9.9	1.1	1.2
25	3.49	161	662	0.86	3	95.3	78.8	37.3
26	3.77	167	220	0.62	14	34.8	2.2	0.7
27	4.57	6	928	0.64	40	95.6	92.9	66.5
28	1.07	149	284	0.70	0	19.4	6.5	8.0
29	0.51	59	441	0.53	153	55.3	27.8	15.5
30	1.84	164	1019	0.94	90	62.0	314.7	534.3
31	1.28	163	272	1.00	0	53.2	5.4	1.6
32	0.86	20	548	0.52	153	56.5	46.7	35.1
33	2.38	176	365	0.59	176	51.1	15.4	7.4
34	3.67	179	477	0.86	82	40.3	21.1	18.8
35	4.28	179	608	0.90	122	28.3	35.0	73.8
36	0.66	191	545	0.63	123	32.3	52.5	86.1
37	2.72	184	294	0.60	153	12.1	8.0	20.9
38	5.54	182	878	0.79	86	67.1	52.5	53.6
39	2.20	194	338	0.82	0	47.2	12.4	5.8
40	2.16	339	166	0.67	0	23.3	1.2	0.6
41	1.57	331	215	0.62	7	17.2	2.7	2.7
42	2.71	192	334	0.67	0	16.2	11.7	24.6
43	1.11	298	240	1.00	45	24.7	39.1	2.7
44	1.34	226	708	0.73	71	43.9	101.1	157.3
45	2.96	200	467	0.66	135	34.9	32.7	38.8
46	2.08	327	227	0.56	27	14.0	3.4	4.9
47	3.25	331	1324	0.90	131	104.5	630.2	749.8
48	3.01	220	740	0.78	122	25.7	129.7	470.3
49	4.02	208	1276	0.87	132	91.2	323.1	414.6
50	2.93	266	711	0.84	23	25.1	116.7	407.7
51	4.26	224	1336	0.88	142	105.5	370.5	412.0

Columns 2 and 3: Position of the hole in polar coordinates in the plane of HoII. The angle θ is measured in degrees and counterclockwise with respect to the receding side (to follow the radio convention of position angle) of the major axis of the galaxy.

Column 4: Diameter of the hole, defined as the geometric mean of the dimensions listed in columns 7 and 8 of Table 5. Here DIAM = (MAJ × MIN)$^{1/2}$.

Column 5: Axial ratio of the hole defined as RATIO = MIN/MAJ.

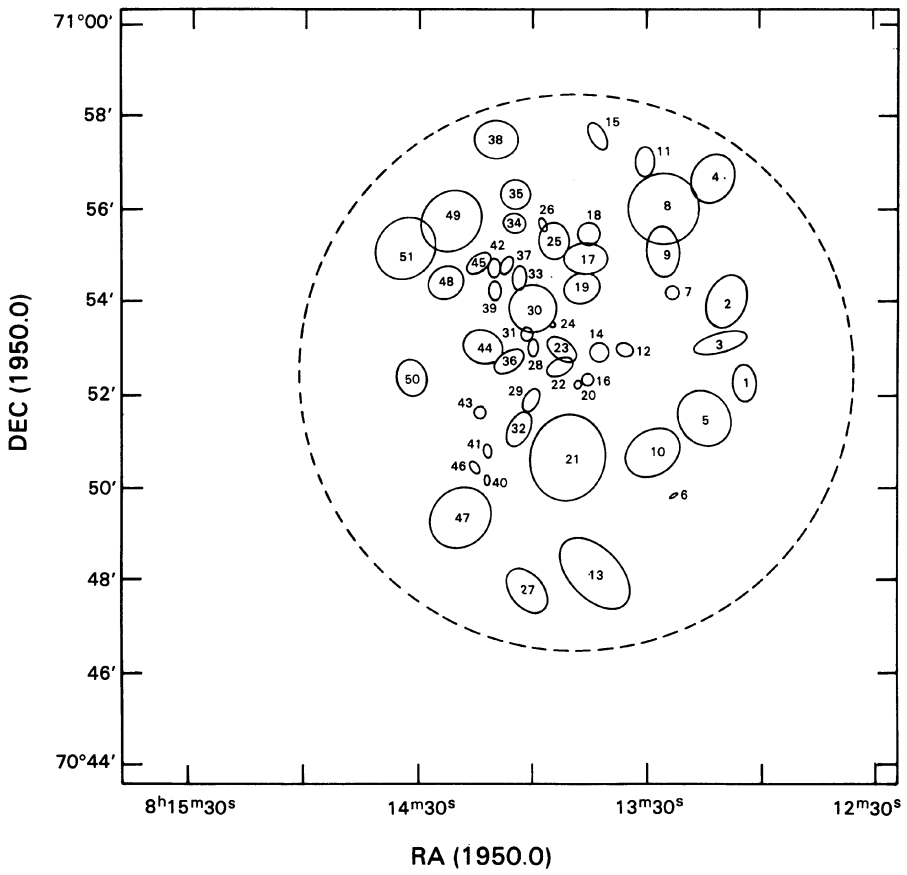

FIG. 12. Location of the holes in HoII.

Column 6: Position angle of the hole. Same as column 9 from Table 5.

Column 7: Kinematic age of the hole in units of 10^6 yr defined as AGE=DIAM/(2×DV).

Column 8: Indicative H I mass in units of $10^4\,\mathcal{M}_\odot$. This is the mass which might have been present at the position of the hole under the assumption that the hole is entirely empty, that $\pi(\mathrm{DIAM})^3/6$ is the characteristic volume of the hole, and that the average volume density corresponds to the density given by the elliptically averaged H I profile given in Table 4 column 4.

Column 9: Energy needed to produce a hole in units of 10^{50} ergs. The expression used to derive the energy is (Heiles 1979):

$$E=5.3\times10^{43}n_{\mathrm{H\,I}}^{1.12}(\mathrm{DIAM}/2)^{3.12}\mathrm{DV}^{1.4}\ \mathrm{ergs}\,. \qquad (1)$$

Where $n_{\mathrm{H\,I}}$ is the average volume density in the disk at the radius of the hole as given in Table 4.

6. STATISTICS OF THE H I HOLES

Figure 12 shows the distribution of the H I holes in HoII. At least 51 different holes have been identified in the total H I map. At first glance it is obvious that the smaller holes dominate the inner parts of the galaxy, the ones being more than ~1000 pc in diameter mostly lying outside of a 2–3 kpc radius. A similar trend was pointed out by Deul & den Hartog (1990) for M33. It is shown for HoII in Fig. 13, where we estimate that 85% of the holes larger than 800 pc are at a distance greater than 3 kpc, while 62% of the smaller holes are inside that radius. The radial number distribution of the holes is presented in Fig. 14.

The number distribution of diameters of the holes is presented in Fig. 15. This figure can be compared with Fig. 8 of BB86. It is obvious that the two distributions are very different. In M31 the distribution peaks at 150–200 pc while in HoII the largest number of holes is found around 500 pc and extends all the way out to 1700 pc. At DIAM > 300 pc HoII has more holes than M31! This may appear counter-intuitive. Why would dwarf galaxies have much larger holes in their interstellar media than large spiral systems? Indeed, the largest complete holes (e.g., the ones that have H I emission seen across the entire face of the shell and consequently have not suffered blow-out conditions) have diameters of 1200–1500 pc. If the holes are nearly spherical in shape then the full extent of the H I layer must be of the same order of magnitude, and hence the scale height, defined as the 1σ value for a Gaussian distribution of H I gas, should be h=600–750 pc. This implies that the scale height of the neutral gas is much larger than in spiral galaxies as, for example, in M31 where it typically measures 170 pc. Since the column densities are

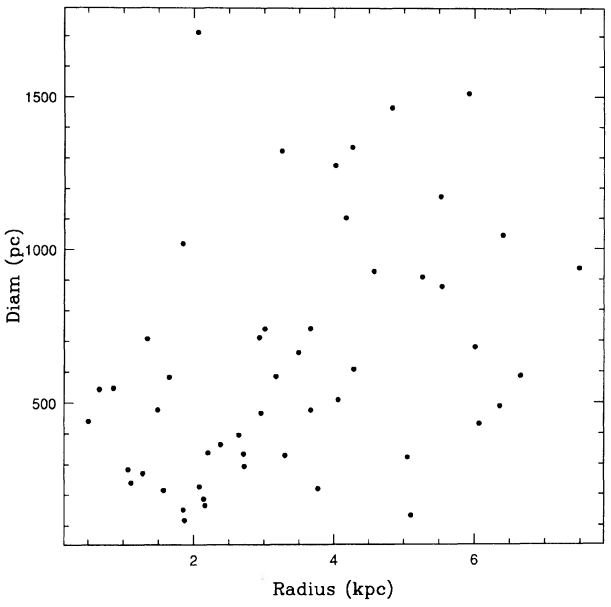

FIG. 13. Diameter vs galactocentric radius for the H I holes.

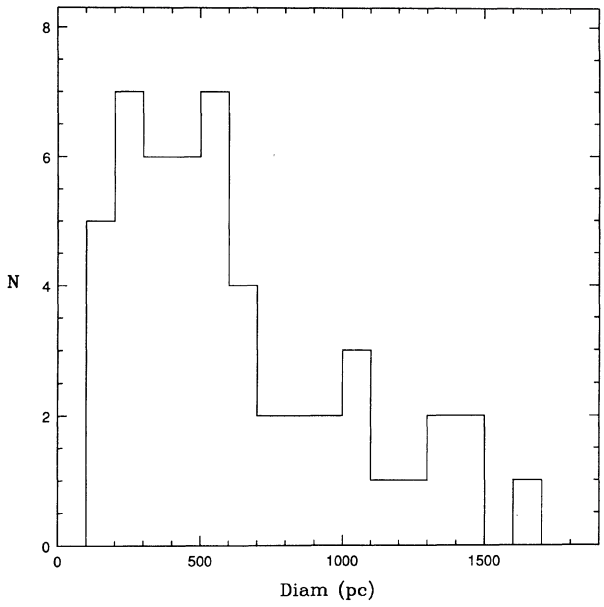

FIG. 15. Number distribution of diameters of the H I holes.

similar to values measured in large spirals, the volume density is lower and facilitates the growth of H I shells to larger sizes. As we will show in Sec. *8.1*, the larger scale height deduced on the basis of the sizes of the H I holes corresponds with that derived from kinematical and stability considerations.

The number distribution of axial ratios is presented in Fig. 16. Since most of the holes are larger than the synthesized beam of the VLA observations (60–70 pc) no contamination is present due to the observed resolution. The average ratio is roughly 0.75, which is higher than the average ratio of 0.60 for the holes in M31 (i.e., the holes in HoII are rounder). The fact that the distribution in Fig. 16 is double peaked is most likely due to low statistics. As can be seen in Fig. 17, not only are the H I holes in HoII rounder in general, but there is a trend with size as well, the bigger holes being slightly more circular. However, one might argue that there is a tendency for the eye to find rounder holes when they are more extended and at a lower surface brightness. Extended elongated structures are more easily discarded as chance alignments or considered to be made up of two smaller structures.

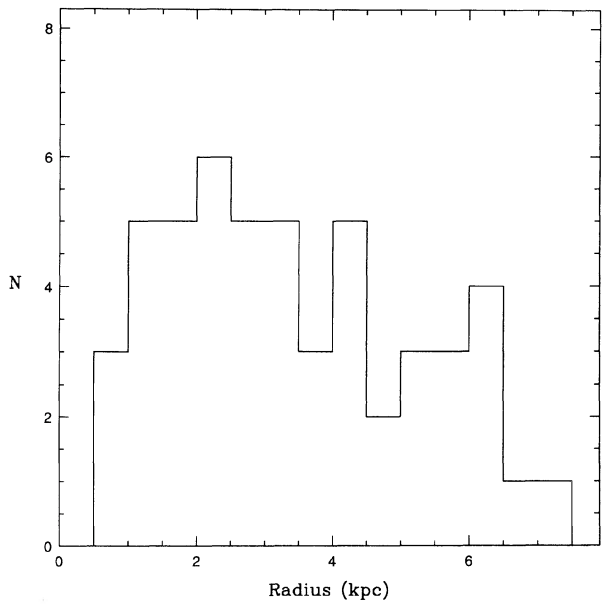

FIG. 14. Radial number distribution of the H I holes.

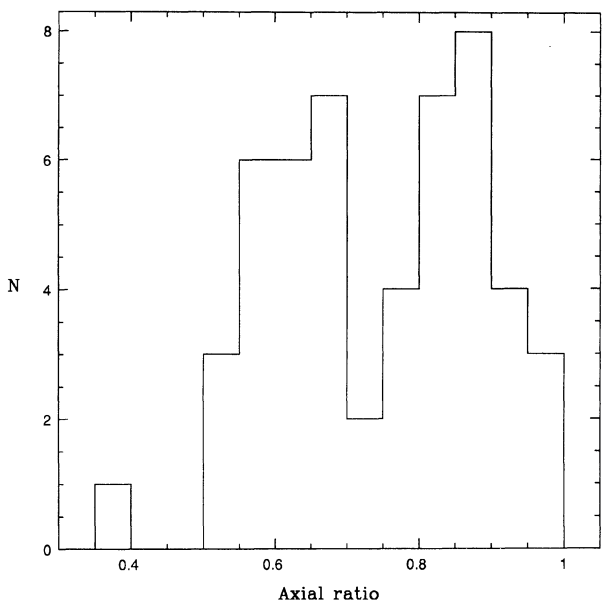

FIG. 16. Number distribution of axial ratios of the H I holes.

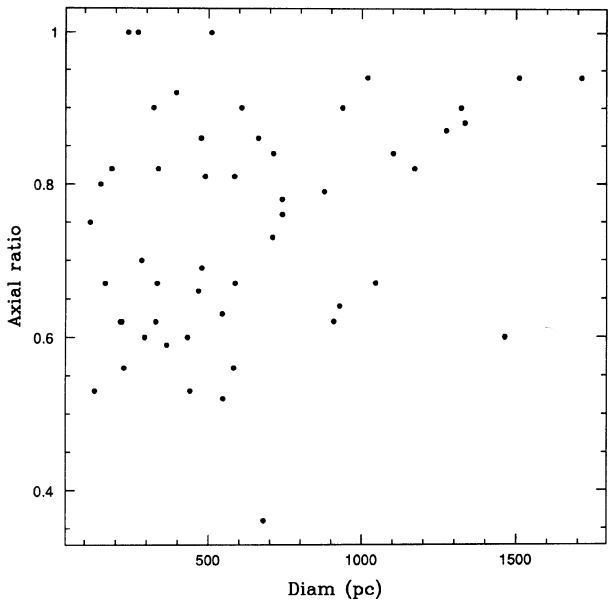

FIG. 17. Axial ratio vs diameter of the H I holes.

The distribution of expansion velocities is shown in Fig. 18. Comparison of these velocities with the values found for M31 suggests that the expansions are systematically lower in HoII. The distribution peaks at around 6 km s^{-1} whereas the maximum in M31 is 10–12 km s^{-1}. In M33, the peak lies between the values for HoII and M31, at around 8 km s^{-1}. An interesting correlation exists in Fig. 19, where the expansion velocities are plotted as a function of diameter of the shells. For small shells the expansion can take any value, but there is a trend for the expansion velocities of the larger shells to converge to a

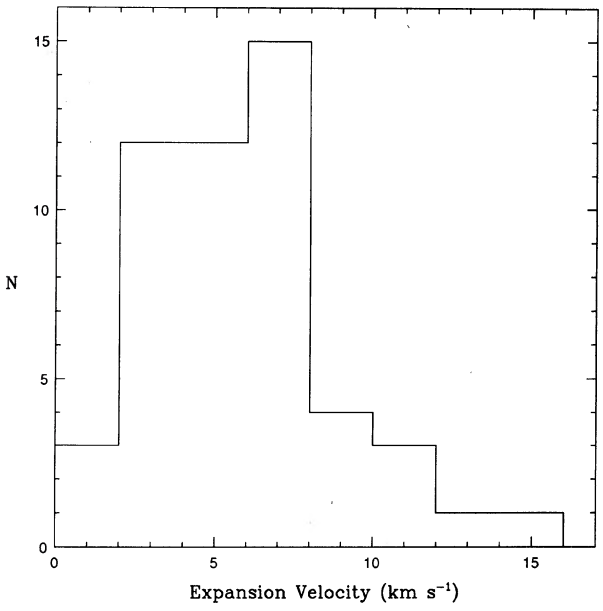

FIG. 18. Number distribution of the expansion velocities of the H I holes.

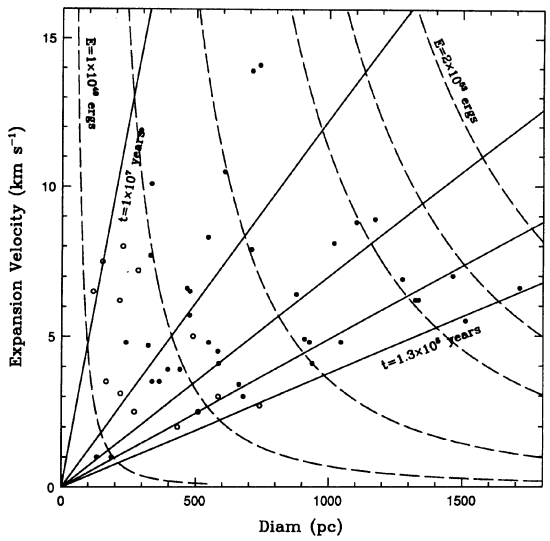

FIG. 19. Distribution of the expansion velocities vs diameter of the H I holes. Open circles are the points where the velocities are questionable. These are indicated by a question mark in column 6 of Table 5. Dashed curves represent values of constant energy of 2.0, 1.0, 0.5, 0.1, 0.01, 0.0001 × 10^{53} ergs. The solid lines represent dynamical ages of 1.3, 1.0, 0.7, 0.4, and 0.1 × 10^{8} yr.

single value. When considering the hydrodynamical model of Chevalier (1974), which describes the evolution of a spherically symmetric supernova remnant, one can derive the expression for the energy requirements of an expanding shell (Heiles 1979). This expression, which we presented in Eq. (1), can be used to draw lines of constant energy on Fig. 19 (dashed lines), where we have assumed an average constant ambient density of $n_{\mathrm{H\,I}} = 0.15$. In the same context, we can use our equation for the age of the holes to draw lines of constant time. With Eq. (20) of Chevalier (1974) the relation for time as a function of radius and expansion velocity can be written as

$$t_5 = 3.04R/v, \qquad (2)$$

where t_5 is the expansion time in units of 10^5 yr, R is in pc and v is in km s^{-1}. This relation gives ages which are systematically 3 times lower than our estimates of age. However, the modeling was made with a single supernova explosion rather than with multiple blasts. Our values in Table 6 are probably an upper limit to the ages of the structures. The most obvious feature is that the holes seem to have a maximum age of $\sim 1.4 \times 10^8$ yr. This might be due to the fact that older holes are sheared by differential rotation or that an event has triggered star formation just over 10^8 yr ago. This question will be discussed in more detail in Sec. *8.3*.

Inspection of the number distributions of Age, Mass, and Energy (Fig. 20) shows that the total kinetic energy transferred to the ISM is similar in HoII and in M31. The only major difference is the ages of the structures, which was already suggested by the number distributions of diameters and expansion velocities. The combined effect of larger sizes and smaller expansion velocities implies that

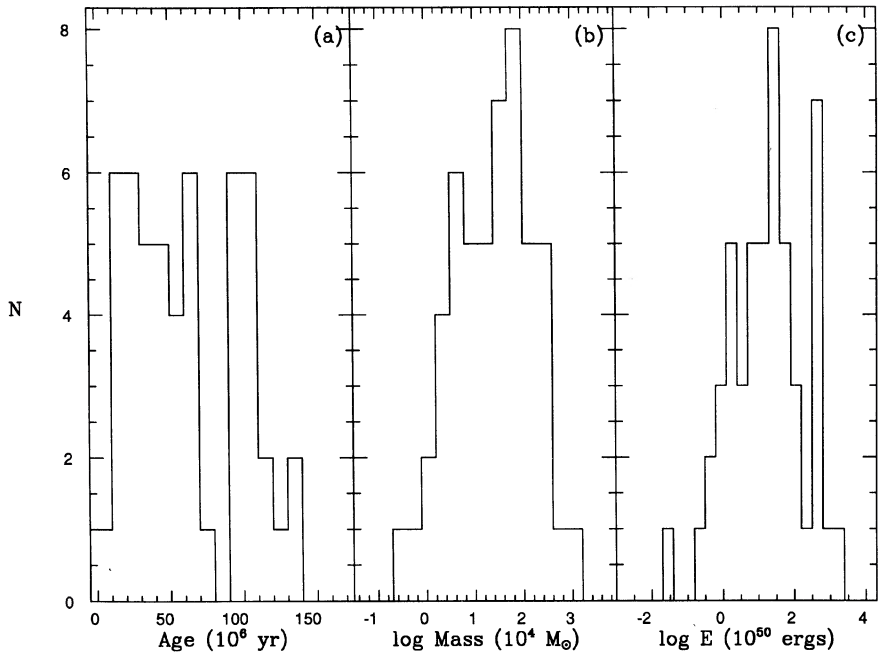

FIG. 20. Number distribution of (a) age, (b) H I mass absent, and (c) energy required to produce the holes.

the bubbles in HoII are older (or longer lived) than in M31. This observation could be explained by taking into account the global effects of density wave passage, shear, and small scale height of the disk in M31, which contribute to make the holes lose their identity more quickly.

7. CORRELATION OF THE H I WITH OPTICAL FEATURES

The most compelling evidence for the stellar wind and supernova origin of the holes comes from a comparison of the H I and Hα data. In Fig. 21 [Plate 110] we have superimposed the full resolution H I data on the Schmidt Hα image of HoII. It is obvious that the Hα emission comes mainly from the high density walls of the large holes, especially where several bubbles intersect. The small H I holes, such as numbers 16, 20, 22, and 43 are filled with Hα emission. There is no Hα emission coming from the interiors of the larger bubbles, indicating that these regions have been either evacuated completely, or their interiors heated to such high temperatures that the emission no longer falls in the visible part of the spectrum. This global comparison, combined with evidence for radial expansion, strongly favors a wind + supernova origin of the holes. Moreover, the morphology of several H II regions is consistent with shock driven shells blown by a hot superbubble which is energized by stellar winds and sequential SNe.

We asked ourselves whether the shell density of electrons in the small holes would correspond to the neutral hydrogen density if the holes were filled with H I emission instead of Hα. The calibrated Hα region which is indicated in Fig. 8, has a flux of 9.54×10^{-13} ergs s^{-1} cm^{-2} over an area of approximately $30'' \times 30''$. With the equation given in Peimbert *et al.* (1975) for the emission measure (EM) determined from the Hα flux,

$$\mathrm{EM} = 2.41 \times 10^3 T^{0.92} I_{\mathrm{H}\alpha}\ \mathrm{cm}^{-6}\ \mathrm{pc}, \quad (3)$$

where $I_{\mathrm{H}\alpha}$ is the Hα flux in units of ergs s^{-1} cm^{-2} sterad^{-1}. Using 10^4 K for the gas temperature, the emission measure in this nebula is EM = 520 cm^{-6} pc. This is low compared to the core of most galactic H II regions (where EM is between 10^3 and 10^4) and more in the range of diffuse optical H II regions. This is likely due to the fact that we are integrating over a large area. If we assume that the proton and electron densities are the same, then the emission measure gives the mean electron density:

$$\mathrm{EM} = N_e^2 L\ \mathrm{cm}^{-6}\ \mathrm{pc}, \quad (4)$$

where N_e is the electron density and L the pathlength in pc through the H II region assumed to be equal to its diameter. From these values we derive an electron density of $N_e \simeq 1$ cm^{-3}. In the inner parts of the galaxy the volume density of the H I gas is of the order of 0.3–0.4 cm^{-3} (Table 4). Considering the uncertainty in the Hα calibration, our lack of knowledge of the filling factors involved, the fact that we have neglected any contribution from gaseous components other than H I, and the uncertainty in the disk scale height, the electron density suggests that most of the H I gas in the Hα-filled holes is ionized. These uncertainties still leave some room for a fraction of the neutral gas to be swept up by the stellar winds and produce an observable expanding shell.

The optical R-band image is shown superimposed on the high resolution H I distribution in Fig. 22 [Plate 111]. In this picture it is obvious that the H I is more extended than the Holmberg radius, which is normal for most gal-

axies. The optical distribution is chaotic with several sites of active star formation. There is no spiral or bar structure readily observable. There is obvious contamination by foreground stars over the entire field. However, at the center of some of the H I structures there are a few stars whose magnitudes (Hoessel & Danielson 1984) are consistent with membership in the HoII system. Most of these turn out to be the brightest stellar objects in HoII with estimated masses of 10–25 $\mathcal{M}_\odot$. It is likely that these objects are single stars. Some of them could be members of the remaining clusters which created the holes. A few of them are H II regions because Hα emission is visible in our CFHT image. Spectroscopic observations should enable us to discriminate between these options.

8. DISCUSSION

In this section we describe the global properties of the H I and optical observations of HoII, and make a comparison with an evolutionary scenario for the interstellar medium in this galaxy. This discussion is based on the complete range of available data on HoII and on some empirical relations inferred from the study of other nearby dwarf galaxies.

8.1 The Mass Distribution in HoII

An analysis of the mass distribution in HoII cannot be complete without having reliable photometry. However, the rotation curve and the global properties of the light and gas distributions can give us some indications of how the different components contribute to the dynamics of the system. The relation

$$\mathcal{M}(r)=2.3265 V_{\max}^2(r) R_{V\max}\times 10^5\ \mathcal{M}_\odot \qquad (5)$$

gives the total mass of a gravitationally bound spherical system. In this equation $R_{V\max}$ is the radius at the last point of the rotation curve in kpc and $V_{\max}$ is the rotation velocity of that point in km s^{-1}. As can be seen from the rotation curve (Table 3), the maximum radius of the disk is at 7.5 kpc and the velocity of this last measured point is 35 km s^{-1}. With these values a total mass of $\sim 2\times 10^9$ $\mathcal{M}_\odot$ is derived. When the total H I mass of 7×10^8 $\mathcal{M}_\odot$, derived in Sec. 3, is corrected (multiplied by 4/3) to account for the He contribution, a total gaseous mass of 9.3×10^8 $\mathcal{M}_\odot$ is obtained. This turns out to be nearly 50% of the total mass. It is difficult to know what the blue mass to light ratio of the disk is for these late-type dwarf systems but a reasonable assumption is that it is around $\sim$1 solar units. With a total blue luminosity of 0.67×10^9 $L_\odot$ (Table 1), we can infer a total stellar mass of $\sim 0.67\times 10^9$ $\mathcal{M}_\odot$. The mass contribution of the optical disk is mostly limited to the inner regions. Nevertheless, these simple calculations indicate that the inner part of the rotation curve can be accounted for very well by the observed mass components, while the outer rotation curve probably needs a contribution from a dark halo.

8.2 The Scale Height of the HI Layer

In column 4 of Table 4 we present an indicative ambient volume density of H I as a function of radius. This was derived from the H I profile and converted to volume density using

$$n_{\rm H\,I}=N_{\rm H\,Ic}/h\sqrt{2\pi}\ \text{cm}^{-3}. \qquad (6)$$

The factor $h\sqrt{2\pi}$ is the effective thickness of the H I layer which is assumed to have a Gaussian profile with a 1σ scale-height h.

The scale height can be calculated in an approximate way using the fact that it should be proportional to the velocity dispersion of the gas and inversely proportional to square root of the mass density in the disk (Kellman 1972; van der Kruit 1981). The scale height of the gas is given by

$$h(r)=\sigma_{\rm gas}/[4\pi G\rho(r)]^{1/2}, \qquad (7)$$

where r is the galactocentric distance. In the absence of reliable photometry for HoII, it is not possible to construct a mass model for this system, which would be necessary to derive the relative mass contributions of the disk components and of the halo as a function of radius. A simple approach is to use the total mass of the galaxy at the last point of the rotation curve and to divide this value by the volume of a sphere of radius $R_{V\max}$. With a total mass of $\sim 2\times 10^9$ $\mathcal{M}_\odot$, the mass density is $\rho\simeq 0.0014$ $\mathcal{M}_\odot$ pc^{-3}. In order to correct for the fact that the density in the disk is in general higher than in the surroundings we take twice the average density and use this value in Eq. (7). For a velocity dispersion, $\sigma_{\rm gas}=6.8$ km s^{-1}, we find a scale height of $h_{\rm HoII}\simeq 625$ pc. This estimate of ρ will be improved when good photometry becomes available and a more complete mass model is made. It is also not possible, at present, to determine the scale height as a function of radius in HoII. There are indications, however, that the scale height of the gas in the inner parts is lower than in the outer parts because of the observed lack of large H I holes near the center. This can be due either to a higher volume density which inhibits expansion, or to the fact that holes suffer blow-out at an early stage (Norman & Ikeuchi 1989). Both explanations require (or indicate) a smaller scale height. A value of $\rho_{\rm disk}\simeq 0.0028$ $\mathcal{M}_\odot$ pc^{-3} is reasonable for a dwarf system (Puche & Carignan 1991, and references therein). Also, any uncertainty on $\rho_{\rm disk}$ enters via the square root, reducing its influence on the determination of the scale-height. In the case of M31, assuming a constant velocity dispersion and the mass model of Emerson (1976), Brinks & Burton (1984) derived the mass density in the disk and hence the scale height as a function of radius. They find that the scale height of H I in M31 gradually increases from 60 pc in the inner parts to about 185 pc at large radii. Applying our crude method to M31, we find a scale height of 170 pc, which is in excellent agreement given our simple approach. As explained in Sec. 3, using $h_{\rm HoII}\simeq 625$ pc for the scale height in Eq. (6) gives us the volume density of H I as a function of radius listed in Table 4.

It is clear that HoII has a gas disk scale height which is significantly larger than that of normal spiral galaxies. This also implies that the volume density of the gas in the disk is low. Both factors contribute to the observed properties of holes in HoII which are larger than in grand-design spirals, first because holes can expand to larger sizes in low density media (see e.g., TTB88, and references therein) and second, because they will not blow out as early as in systems with smaller scale height (Tenorio-Tagle *et al.* 1990; Tomisaka 1991). There is some evidence that the gas disks of dwarf galaxies are much thicker than those of larger spiral systems. Their aspect ratio is of the order 10:1 rather than 100:1 which implies that it is difficult to find edge-on dwarf irregulars on the basis of their morphology alone. As the rotation curve is often close to solid body, no clues regarding their inclinations are given by mapping their velocity fields. Both effects explain the lack of edge-on dwarf irregulars in various catalogues of galaxies. Bottema *et al.* (1986); using the Westerbork telescope, observed the edge-on dwarf galaxy NGC 5023, which has an apparent axis ratio of 0.15 (de Vaucouleurs *et al.* 1976). They find that the H I gas layer has a scale height of 460 pc for an assumed distance of 8 Mpc based on a Hubble constant of 75 km s^{-1} Mpc^{-1}. This system is more massive than HoII with a maximum rotation velocity of $\sim$80 km s^{-1}.

8.3 Evolution of the Bubbles

Let us now focus our attention on the interpretation of the phenomena responsible for the appearance of HoII. The shell-like structures that are so obvious in the H I and Hα distributions clearly originate from strong localized energetic events in the interstellar medium. The energy needed to produce these structures could come from forces within the disk itself or external events acting on the disk. In the latter case the infall of intergalactic clouds, or HVCs, has been invoked as a possible mechanism for blowing holes in the ISM. This mechanism is suggested for the production of the biggest holes seen in M101 (van der Hulst & Sancisi 1988). However, HoII is fairly isolated in space, and the distribution of the holes in its disk is too regular and omnipresent at all radii to be explained by infall. Also, since some of the holes must have been formed only recently it is reasonable to assume that infalling gas would be visible in the form of high velocity clouds in many regions of the disk, as in M101. This is not seen in our H I data, nor do we have any indication for low mass intergalactic H I clouds except for the large one seen to the southwest of HoII.

The theoretical framework for the formation and evolution of the bubbles in the ISM is well established. The observed parameters needed for a comparison with theory are the mass of the expanding shell, its velocity, its size, and the density and metallicity of the ambient medium into which the shell propagates (TTB88). Several other observables should be included in this list which could allow us to distinguish between competing sources of energy for the shells. Among these are soft x-ray observations of the regions within the shells, spectrophotometric observations of the near stellar objects found at the center of the bubbles, molecular gas observations in and around the supershells, etc. In this section we discuss some of these observational tests and how they apply to the case of HoII.

From the observed radial expansion (Figs. 9–11), energy requirements, distribution, and kinematic ages of the H I holes in HoII, we can assume that the shells originate from internal, pressure driven events. TTB88 have used the global model of the ISM of Larson (1987, 1988) to propose an evolution cycle for the ISM with star-formation epochs which are self-propagating and self-regulating. We use the Tenorio-Tagle and Bodenheimer model to make predictions about the structure and evolution of the ISM and see where it is successful and where it fails. In this model, the onset of star formation is the first phase transition from a smoothly distributed ISM. In the absence of a gravitational instability, which can grow from a very small local perturbation, a triggering mechanism is needed for the first events to occur. In dwarf galaxies, one plausible trigger is an encounter with a massive object such as another galaxy. HoII is associated with the larger spirals NGC 2403–M81, and a dynamical timescale for interactions can thus be derived from the crossing time. Since HoII is a member of the group without being close to either of the two galaxies, values of crossing times range from 1 to 5 $\times$ 10^9 yr. This is much longer than the expansion time of even the largest holes (about 10^8 yr). Therefore, if interaction is the source of the starburst, we are not witnessing the first generation of stars. This is consistent with the heavy element abundance and star-formation rate in this system (Hunter & Gallagher 1985); the abundances are comparable to those found in the LMC, while the mass and blue luminosity of HoII are similar to those of the SMC.

The second phase happens when the newly formed OB stars enter the main sequence. The massive production of ionizing photons results in a visible H II region and causes the disruption of the parent molecular cloud. The combined stellar winds of the most massive stars generate a hot bubble which drives an outward expanding shell of H II gas. Several of the H II regions of HoII may be in this phase (Fig. 8). It is obvious that the largest holes have very little Hα emission in their interior while the smallest are, as shown in Sec. 7, filled with ionized gas. We determined that the electron density, derived from the Hα emission, is compatible with most of the H I being ionized. This suggests that the smallest holes are in the ionization phase where young OB stars are still on the main sequence or not far evolved.

As the O and B stars leave the main sequence, they become red supergiant stars with a much reduced effective temperature. Thus HoII should contain many giant and supergiant stars, particularly in the regions of the small H I holes. This is consistent with Hoessel & Danielson (1984) who found that HoII has a comparatively large number of red supergiants. However several of the "red supergiant stars" in their list correspond to small H II regions on the Hα images. Therefore they may not be supergiants. It would be extremely useful to be able to distinguish between

main sequence O and B stars, H II regions, and supergiant A and F stars, but the fact that O and B stars should be in denser environments rather than in the blown-out cavities surrounding A and F supergiants might render a differentiation on color alone difficult if not impossible. This is an area where spectrophotometry of HoII would be valuable in understanding the evolutionary state of the brightest stars.

Next, a critical stage occurs when the most massive stars deposit a large quantity of kinetic energy into the ISM by exploding as supernovae, creating large-scale expanding shells (Weaver *et al.* 1977; Dorland *et al.* 1986; McCray & Kafatos 1987; Norman & Ikeuchi 1988). This event also leads to the production of hot gas that should be visible in x-rays long after the last supernovae have gone off, and to the creation of Cosmic Ray electrons which are responsible for the nonthermal radio emission. According to the analytic models of McCray & Kafatos (1987), the pressure created by the hot gas will push material outwards until the overpressure is lost when the remnant grows to a size larger than the scale height of the galactic disk gas (see also the numerical models of Tenorio-Tagle *et al.* 1990). The rate of growth and the size of the shells are highly dependent on the density of the cool gas (Heiles 1990; TTB88). A galactocentric radial dependence of the size distribution of the holes is an obvious feature in HoII (Fig. 13). Smaller holes tend to be in the inner regions of the galaxy while all the larger holes lie in the outer regions. A similar dependence was recognized by Deul & den Hartog (1990) in M33. They attributed this to the presence of inter-arm regions in the outer parts of the galaxy. A second possibility is that the density of the H I disk decreases in the outer regions which facilitates expansion. One can look at the H I radial distribution in HoII and assume a constant scale height for the disk. The small holes are found, although not exclusively, in the constant density inner regions of the disk, whereas the big holes are found at larger radii where the volume density of the gas diminishes by a factor of 3–10. If the disk is allowed to flare up in the outer regions, as is normally the case in spirals, then the volume density becomes even smaller, allowing for yet easier expansion.

The rotation curve presented in Fig. 6 allows us to determine a rotational period for the gas. Since the rotation curve is nearly flat throughout most of the extent of the disk, a global timescale can be derived which turns out to be $t_{\rm rot} \simeq 8 \times 10^8$ yr at a radius of 5 kpc. This time is an order of magnitude larger than the expansion timescale of the largest holes. However, the amount of shear over 1 or 2 kpc in radius is sufficient to stretch the holes to an axial ratio of 0.5 over a timescale of 10^8 yr. This might explain very well why a cutoff for the observed ages of the holes is observed in Fig. 19. In faster rotators, like large spiral galaxies, it is obvious that the biggest holes rapidly loose their identity. A nice presentation of the effect of shear on the evolution of holes, applied to M31 and M33, is given by Palouš *et al.* (1990). They find that for galaxies with larger rotation velocities (i.e., larger masses) the identification of big holes is difficult. The distribution of sizes should follow the mass of the parent galaxy. Indeed, if one compares the size distributions of the holes in M31, M33, and HoII, one can see this trend, but more galaxies need to be observed at high resolution before reaching any definitive conclusions. These arguments are corroborated by our finding that on average holes in HoII tend to be rounder than, for example, in M31 (see Figs. 16 and 17), and that larger holes are primarily found in the outer regions, where shear is less important (because the rotation curve is flat).

It should be noted that in this discussion (as well as in most theoretical models for that matter) the influence of magnetic fields is neglected. Global magnetic fields in the disk of a galaxy would inhibit the expansion of a supernova driven bubble in directions perpendicular to the field lines. The expansion along field lines would not be affected resulting in elongated structures (Tomisaka 1991). The fact that H I holes in HoII are so nearly spherical can be used to argue that magnetic fields do not play an important role. Again, multifrequency radio continuum observations will be important to assess the strength of the magnetic field based on the nonthermal emission.

It was reported in Sec. 5 that the bubble walls exhibit velocity profiles which are broader than the quiescent regions. Simply taking these dispersions to reflect kinetic temperatures predicts the neutral hydrogen has a mean temperature of approximately 25 000 K, much too hot to remain neutral. We interpret this as an indication that the velocity dispersions are due to turbulence or the velocity distribution of individual clouds. Turbulence by itself would eventually heat the gas to nearly the same temperature, opening the question of the fractional volume of HoII filled by H I clouds. We are unable to determine this filling factor with our data.

Tenorio-Tagle (1987) has reported test calculations which produce broadened shells with a large velocity dispersion and a low compression factor. From our high resolution H I data it is obvious that the walls of the shells are several resolution elements in thickness corresponding to several hundred pc. The shells exhibit overdensities which are not very high above the more uniform background. These observed properties of the shells fit very well with the above-mentioned model calculations, which are based on a multiple supernova explosion scenario.

As the expanding bubble sweeps up more and more gas, the density of the shell in the disk increases until gravitational instabilities lead to molecular cloud formation, most likely in the shocked gas present at the intersections of the bubbles (Palouš *et al.* 1990). One can try to quantify this and find whether the column density is sufficient to shield the cloud against the external UV radiation field. The minimum column density as a function of metallicity (Franco & Cox 1986) is

$$N_{\rm opacity} = 10^{21} \left(\frac{Z_\odot}{Z}\right) \rm cm^{-2}. \quad (8)$$

We know from Hunter & Gallagher (1985) that $Z_{\rm HoII} \simeq 0.4 Z_\odot$ implying a minimum column density of 2.5×10^{21} cm^{-2} for shielding of the radiation field. This condition implies a density contrast for the shell over the av-

erage background of only a factor of 3 in the inner regions of HoII. However, in the outer disk a more extended region needs to be swept up in order to allow the H I clouds to be massive enough to favor the formation of molecular material.

If one assumes that star formation follows spontaneously from molecular cloud formation, then the cycle is complete and secondary star formation is self-regulated. The superposition of the Hα image and the integrated H I in HoII displays secondary star formation in a striking fashion. Not only is most of the Hα emission distributed along the walls of the shells or in the dense inner regions of the galaxy, but also the small holes are filled with the Hα emission remaining from the ionized, wind-blown cavity around the young O and B stars. Because the abundance in HoII is lower than in M31 or M33 one expects more massive stars to be formed, hence the correlation of the Hα and the H I to be tighter. This implies that a different IMF could be at work in HoII. The photometric data from Hoessel & Danielson (1984) already gives the indication that an unusually large number of massive stars is present in HoII.

8.4 What Fills the Holes?

An obvious question about the evolution of the holes in HoII is: what fills the holes? If supernova explosions are the main source of energy for the pressure driven expansion of the holes, then hot (10^6 K) gas should be left behind (de Young & Gallagher 1990). The long cooling time of this low density medium should allow it to be observable as a background of soft x-ray emission. No direct pointed x-ray observations have yet been obtained on HoII. However, several authors (Singh *et al.* 1987; Chu & Mac Low 1990; Wang & Helfand 1991; Wang *et al.* 1991) used data obtained from the *Einstein* satellite to find that several large holes in both the H I and visible light distribution of the LMC were filled with soft x-ray emission. Until more x-ray, and possibly molecular observations are obtained of HoII it will be impossible to know with certainty what fills its holes. However, the supernova explosion scenario seems the most plausible at this time.

8.5 On the High Values of T_B

The high resolution cube shows very high surface brightnesses for several of the shells. These high peak brightness temperature regions coincide with the peak Hα emission at the intersection of the largest holes. Brightness temperatures of the 21 cm line are derived to be between 150 and 250 K. In the Galaxy, peak brightness temperatures never exceed 120 K. Higher peak brightness temperatures were recently reported to be present in the high resolution H I imaging of M31 by Braun & Walterbos (1991). Draine (1978) showed that a high dust-to-gas ratio or a high ionization rate lead to high temperatures in the cool ISM, a high gas phase metallicity or high gas pressure lead to lower temperatures. Compared to the Galaxy, M31 has a similar dust-to-gas ratio, a higher metallicity, and a lower ionization rate due to its lower star-formation rate and lower radio continuum power. In order to explain the higher peak brightness temperatures, this led Braun & Walterbos (1991) to propose a lower gas pressure in M31.

An alternative interpretation was suggested by Dickey (1991) and Dickey & Brinks (1992), who ascribe the higher peak brightness temperatures to a different contribution along the line of sight for the warm and cool phases of H I. M31 is seen nearly edge-on, so when one assumes that the warm gas has a larger scale height, as is the case for the Galaxy, a line of sight will traverse a larger column of warm gas before hitting an optically thick cloud in the disk, thus raising the peak brightnesses. In their description, the temperature of the cool H I and the fraction of cool versus warm gas are taken to be the same in M31 as in the Galaxy.

In HoII several factors might contribute to explain the observed peak brightness temperatures. The average metallicity in a number of H II regions is low, comparable to the metallicity of the LMC (Hunter & Gallagher 1985). The star-formation rate in HoII is higher than, for example, in M31. This suggests a high ionization level, as does the 20 cm radio continuum emission (Condon 1987). The global dust-to-gas ratio might be quite low in HoII, which was detected in the *IRAS* faint source catalog. Hunter *et al.* (1986) present *IRAS* images based on pointed observations using the survey instrument and give the infrared fluxes for this system. However, the derived value of $\mathcal{M}_d/\mathcal{M}_{H\,I} \simeq 0.2 \times 10^{-4}$ might not be representative of individual H II regions because of the limited resolution of the *IRAS* observations. The gas pressure of the cool component of the ISM in HoII is likely smaller than the pressure in M31, considering that the scale height of the gas is quite large (this assumes that most of the pressure is caused by gravitation rather than determined by processes related to the evolution of massive stars such as supernova explosions). Therefore the combined effects of a low metallicity, high ionization rate, and low gas pressure might be at the origin of the high brightness temperatures seen in the H I.

On the other hand, the low volume density of H I implies a low volume density of cool gas which in turn means that even if the spin temperature in HoII were the same as in the Galaxy, the line-of-sight averaged opacity $\langle\kappa\rangle$ (Dickey & Brinks 1992) is lower by a factor of 2–3. In that case the mean free path before hitting an optically thick cloud becomes as large as 2.8 kpc, meaning that HoII is virtually optically thin. Note that increasing the spin temperature, as suggested above, decreases the opacity even further. Without the possibility of making H I absorption line measurements due to the lack of suitable background sources, it is impossible to know if the spin temperature in HoII, or dwarfs in general, is substantially different from that of a larger system.

9. CONCLUSIONS

This paper presents high resolution H I and Hα imaging of the dwarf irregular galaxy HoII. The main conclusions can be summarized as follows:

(1) Low surface brightness H I emission is observed over a $\sim 15'$ diameter region in HoII. The low resolution velocity field shows a regular pattern with a symmetrical warping of the H I layer in the outer regions. The total H I mass derived from the integrated intensity is $\sim 7\times 10^8$ $\mathcal{M}_\odot$. The rotation curve is measured out to 7.5 kpc. It shows a rapid rise in the inner parts out to a radius of ~ 2.5 kpc, after which it stays at a fixed level to the last measured velocity point. The maximum rotation velocity is ~ 40 km s^{-1}. The total mass, derived at the last point of the rotation curve, is 2×10^9 $\mathcal{M}_\odot$. Thus HoII has about 50% of its mass in the form of gas.

(2) Large scale (nearly circular) empty structures are prominent in the VLA H I high resolution maps. These H I holes are distributed across the entire face of the galaxy, larger holes exist mostly at large galactocentric distances where the density is low. Holes are seen to be expanding. Observed expansion velocities range between 1 and 15 km s^{-1} which leads to kinematic ages of the structures ranging from 1.0×10^7 to 1.5×10^8 yr. Higher velocities, which should be present in very small holes, are not observed because of our limited spatial resolution. The holes would be longer lived in dwarf galaxies than in larger spirals, which we attribute to the fact that shear due to differential rotation is less significant. This is corroborated by our finding that holes in HoII tend to be rounder.

(3) The radial expansion of the holes and the energy requirements for their formation favor sequential supernova explosions in a preexisting wind blown bubble. A simple spherically expanding shell model can account for the distribution of expansion velocities as a function of radius.

(4) With several reasonable assumptions about the mass distribution in HoII, the scale height of the disk can be calculated from the velocity dispersion of 6–7 km s^{-1} and the mass density in the disk ($\rho = 0.0028$ $\mathcal{M}_\odot$ pc^{-3}), and its value is $h \simeq 625$ pc. This large scale height is consistent with the sizes of the largest H I shells.

(5) There is a striking correlation between the H I shells and Hα emission. The emission measure, calculated from the Hα flux, suggests that the small holes are filled with ionized gas. No Hα is detected from the center of the largest holes, but star formation could be taking place along their perimeter. More photometry is needed to confirm this. Broadband optical images suggest the presence of evolved supergiant stars at the centers of the largest holes.

(6) High peak brightness temperatures of up to 250 K are found near some bright H I/H II region complexes. These high temperatures could be attributed to the combined effect of high interstellar radiation field and inefficient cooling due to low abundance of heavy elements in HoII. On the other hand, the low volume density of cool gas and the long path length through the warm ISM might produce the observed effect.

In summary, HoII seems to fit very well the description given for the evolution of the ISM in galaxies by TTB88. Several of their evolutionary phases can be traced in this dwarf system. The large structures in the ISM can be understood in a natural way once one accepts that the scale height in this galaxy, and possibly in dwarfs in general, is much larger than in regular gas-rich spirals.

Several follow-up studies, such as searches for x-ray emission from the interiors of the bubbles, a VLA multifrequency radio continuum study, and optical spectroscopy of stellar objects, are needed. These are expected to provide valuable additional information on this fascinating object.

We would like to thank the technical staff of the NRAO for helping with the radio observations. The Schmidt telescope time was made available by Dr. Peter Pesch of the Case Western Reserve University. We appreciate the support of the NOAO staff especially Bill Schoening. We are also grateful for the CFHT support. We would like to thank Rick Fisher, John Dickey, Bruce Elmegreen, Esteban Bajaja, and Allan Sandage for helpful comments and lively discussions. We thank Carl Heiles for refereeing this paper and for pointing out changes which greatly improved the manuscript. We thank Theresa McBride and Kathryn Campbell for help with the art work. The research of J.R.R. is supported by a grant from the National Sciences and Engineering Research Council (Canada). This research has made use of the NASA/IPAC Extragalactic Database (NED) which is operated by the Jet Propulsion Laboratory, California Institute of Technology, under contract with the National Aeronautics and Space Administration.

REFERENCES

Aaronson, M., & Mould, J. 1983, ApJ, 265, 1
Baars, J. W. M, Genzel, R., Pauliny-Toth, I. I. K., & Witzel, A. 1977, A&A, 61, 99
Begeman, K. 1989, A&A, 223, 47
Belley, J., & Roy, J. R. 1992, ApJS, 78, 61
Bottema, R., Shostak, G. S., & van der Kruit, P. C. 1986, A&A, 167, 34
Bottinelli, L., Gougenheim, L., Paturel, G., & de Vaucouleurs, G. 1984, A&AS, 56, 351
Braun, R., & Walterbos, R. A. M. 1991, ApJ, 386, 120
Brinks, E. 1981, A&AL, 95, L1
Brinks, E., & Burton, W. B. 1984, A&A, 141, 195
Brinks, E., & Bajaja, E. 1986, A&A, 169, 14 (BB86)
Brinks, E. 1990, in The Interstellar Medium in Galaxies, edited by H. A. Thronson, Jr. and J. M. Shull (Kluwer, Dordrecht), p. 39
Cash, W., Charles, P., Bowyer, S., Walter, F., Garmire, G., & Riegler, G. 1980, ApJ, 238, L71
Chevalier, R. A. 1974, ApJ, 188, 501
Chu, Y.-H., & Mac Low, M.-M. 1990, ApJ, 365, 510
Condon, J. J. 1987, ApJS, 65, 485
Coltrell, G. A. 1976, MNRAS, 177, 463
Cox, D. P., & Smith, B. W. 1974, ApJ, 189, L105
Davis, L. E., & Seaquist, E. R. 1983, ApJS, 53, 269
de Vaucouleurs, G. 1978, ApJ, 224, 710
de Vaucouleurs, G., de Vaucouleurs, A., & Corwin, Jr., H. G. 1976, Second Reference Catalogue of Bright Galaxies (University of Texas Press, Austin)
de Young, D. S., & Gallagher, J. S. 1990, ApJ, 356, L15
Deul, E. R., & den Hartog, R. H. 1990, A&A, 229, 362

Dickey, J. M. 1991, in The Interpretation of Modern Synthesis Observations of Spiral Galaxies, edited by N. Duric and P. C. Crane (ASP, San Francisco), p. 163
Dickey, J. M., & Brinks, E. 1992, in Evolution of Interstellar Matter and Dynamics of Galaxies, edited by W. B. Burton, P. O. Lindblad, and J. Palouš (Cambridge University Press, Cambridge) (in press)
Dorland, H., Montmerle, T., & Doom, C. 1986, A&A, 160, 1
Draine, B. T. 1978, ApJS, 36, 595
Emerson, D. T. 1976, MNRAS, 176, 321
Franco, J., & Cox, D. P. 1986, PASP, 98, 1076
Field, G. B., Goldsmith, D. W., & Habing, H. J. 1969, ApJ, 155, L149
Freedman, W. L., & Madore, B. F. 1988, ApJL, 332, L63
Heiles, C. 1979, ApJ, 229, 533
Heiles, C. 1984, ApJS, 55, 585
Heiles, C. 1990, ApJ, 354, 483
Hoessel, J. G., & Danielson, G. E. 1984, ApJ, 286, 159
Huchtmeier, W. K., & Richter, O. G. 1986, A&AS, 63, 323
Huchtmeier, W. K., & Richter, O. G. 1988, A&A, 203, 237
Humphreys, R. M., Aaronson, M., Lebofsky, M., McAlary, C. W., Strom, S. E., & Capps, R. W. 1986, AJ, 91, 808
Hunter, D. E., & Gallagher III, J. S. 1985, ApJS, 58, 533
Hunter, D. E., Gillett, F. C., Gallagher III, J. S., Rice, W. L., & Low, F. 1986, ApJ, 303, 171
Jacoby, G. H., Ciardullo, R., Ford, H. C., & Booth, J. 1989, ApJ, 334, 704
Kellman, S. A. 1972, ApJ, 175, 353
Kennicutt, Jr., R. C. 1978, Ph.D. thesis, University of Washington
Kulkarni, S. R., & Heiles, C. 1987, in Interstellar Processes, edited by D. J. Hollenbach and H. A. Thronson, Jr. (Reidel, Dordrecht), p. 87
Kulkarni, S. R., & Heiles, C. 1988, in Galactic and Extragalactic Radio Astronomy 2nd ed., edited by G. L. Verschuur and K. I. Kellermann, (Springer, New York), p. 95
Larson, R. B. 1987, in Starbursts and Galaxy Evolution, edited by T. X. Thuan, T. Montmerle, and J. Tran Thanh Van (Frontieres, Gif sur Yvette, France), p. 467
Larson, R. B. 1988, in Galactic and Extragalactic Star Formation, edited by R. E. Pudritz and M. Fich, (Reidel, Dordrecht), p. 459
Martin, P., Roy, J. R., Noreau, L., & Lo, K. Y. 1989, ApJ, 345, 707
McCray, R., & Kafatos, M. 1987, ApJ, 317, 190
Norman, C. A., & Ikeuchi, S. 1989, ApJ, 345, 372
Palouš, J., Franco, J., & Tenorio-Tagle, G. 1990, A&A, 227, 175
Peimbert, M., Rayo, J. F., & Torres-Peimbert, S. 1975, RMxA, 1, 289
Puche, D., & Carignan, C. 1991, ApJ, 378, 487
Rots, A. H. 1980, A&AS, 41, 189
Sandage, A. 1984, AJ, 89, 621
Singh, K. P., Nousek, J. A., Burrows, D. N., & Garmire, G. P. 1987, ApJ, 313, 185
Tenorio-Tagle, G. 1987, in Starbursts and Galaxy Evolution, edited by T. X. Thuan, T. Montmerle, and J. Tran Thanh Van (Frontieres, Gif sur Yvette, France), p. 37
Tenorio-Tagle, G., & Bodenheimer, P. 1988, ARA&A, 26, 145 (TTB88)
Tenorio-Tagle, G., Franco, J., Bodenheimer, P., & Różyczka, M. 1987, A&A, 179, 219
Tenorio-Tagle, G., Różyczka, M., & Bodenheimer, P., 1990, A&A, 237, 207
Thuan, T. X., & Martin, G. E. 1981, ApJ, 247, 823
Tully, R. B. 1988, in Nearby Galaxies Catalog, edited by R. B. Tully (Cambridge University Press, New York)
Tomisaka, K. 1991, in The Interstellar Disk-Halo Connection in Galaxies, IAU Symposium No. 144, edited by H. Bloemen (Kluwer, Dordrecht), p. 407
van Albada, T. S., Bahcall, J. N., Begeman, K., & Sancisi, R. 1985, ApJ, 295, 305
van der Hulst, T., & Sancisi, R. 1988, AJ, 95, 1354
van der Kruit, P. C. 1981, A&A, 99, 298
van Langevelde, H. J., & Cotton, W. D. 1990, A&A, 239, L5
Wang, Q., & Helfand, D. J. 1991, ApJ, 370, 541
Wang, Q., Hamilton, T., Helfand, D. J., & Wu, X. 1991, ApJ, 374, 475
Weaver, R., McCray, R., Castro, J., Shapiro, P., & Moore, R. 1977, ApJ, 218, 377

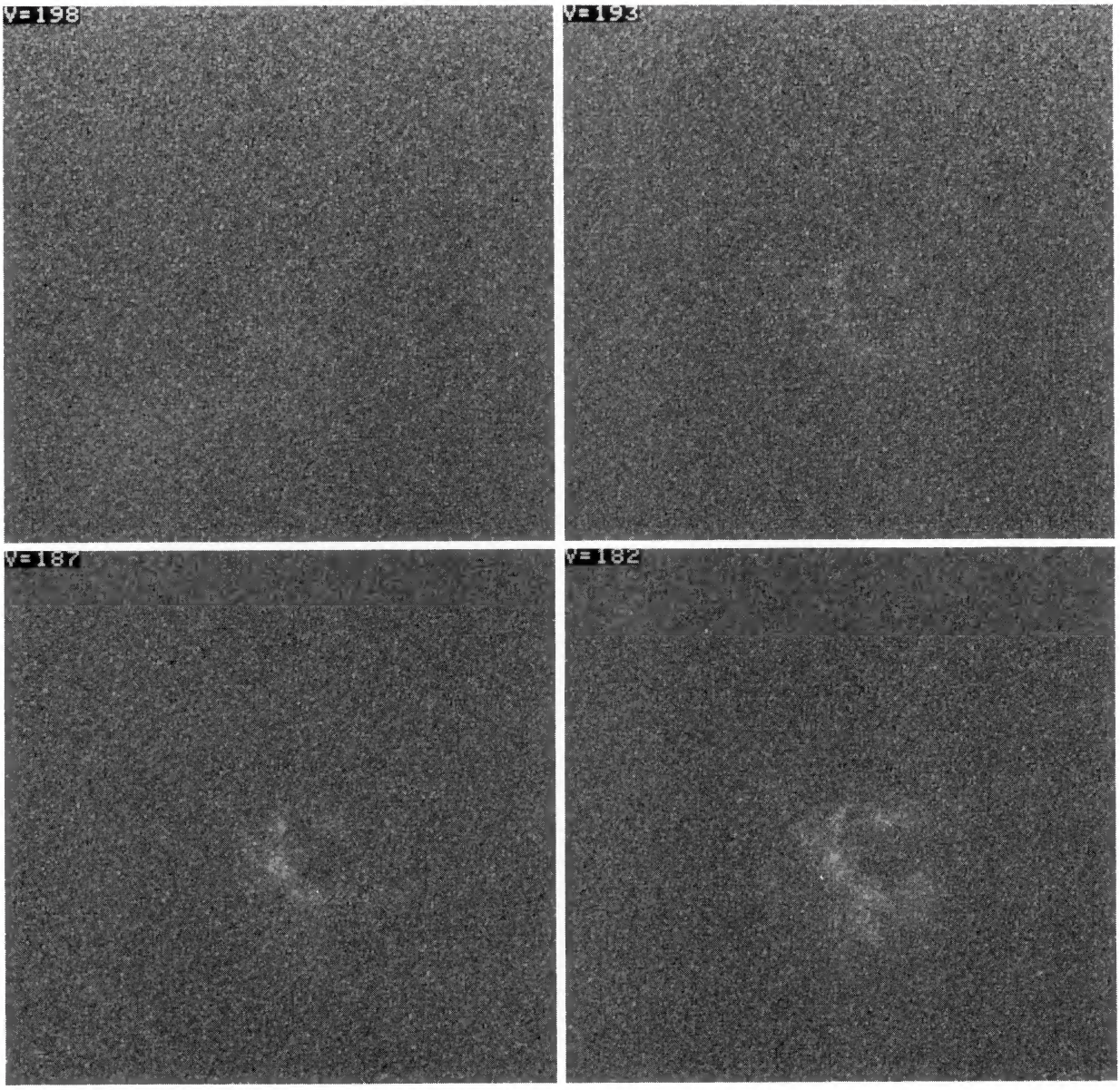

FIG. 1. Mosaic of H I line channel maps at a resolution of 4.0″×4.5″. Each pannel is 17′×17′ centered at $\alpha(1950) = 8^h14'06''$, $\delta(1950) = 70°52'$. The channel width is 2.6 km s^{-1}. The heliocentric velocities of each channel are indicated in the upper-left-hand corner. The maps show the distribution of H I brightness temperature in each velocity channel.

Puche *et al.* (see page 1843)

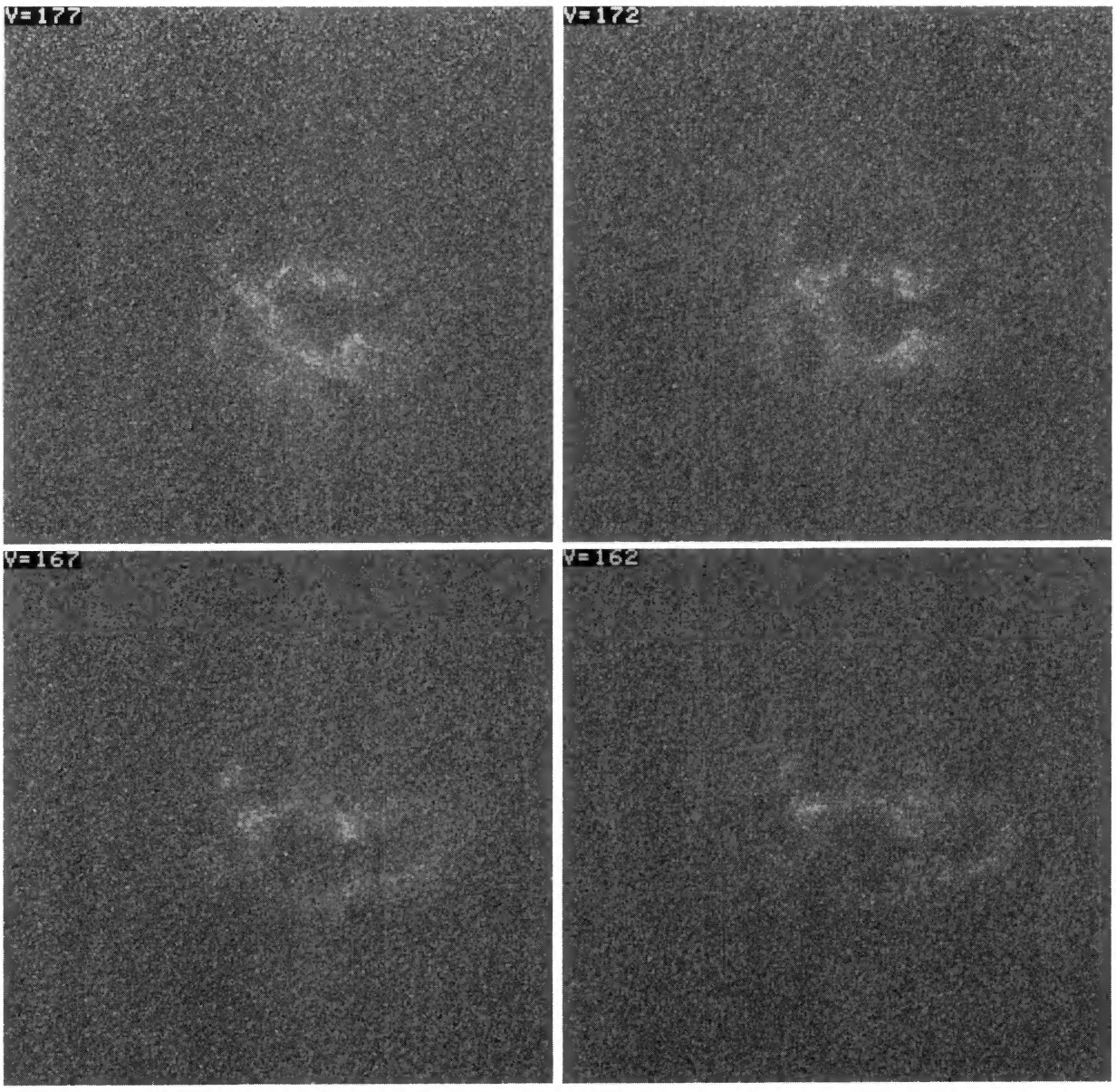

FIG. 1. (continued)

Puche *et al.* (see page 1843)

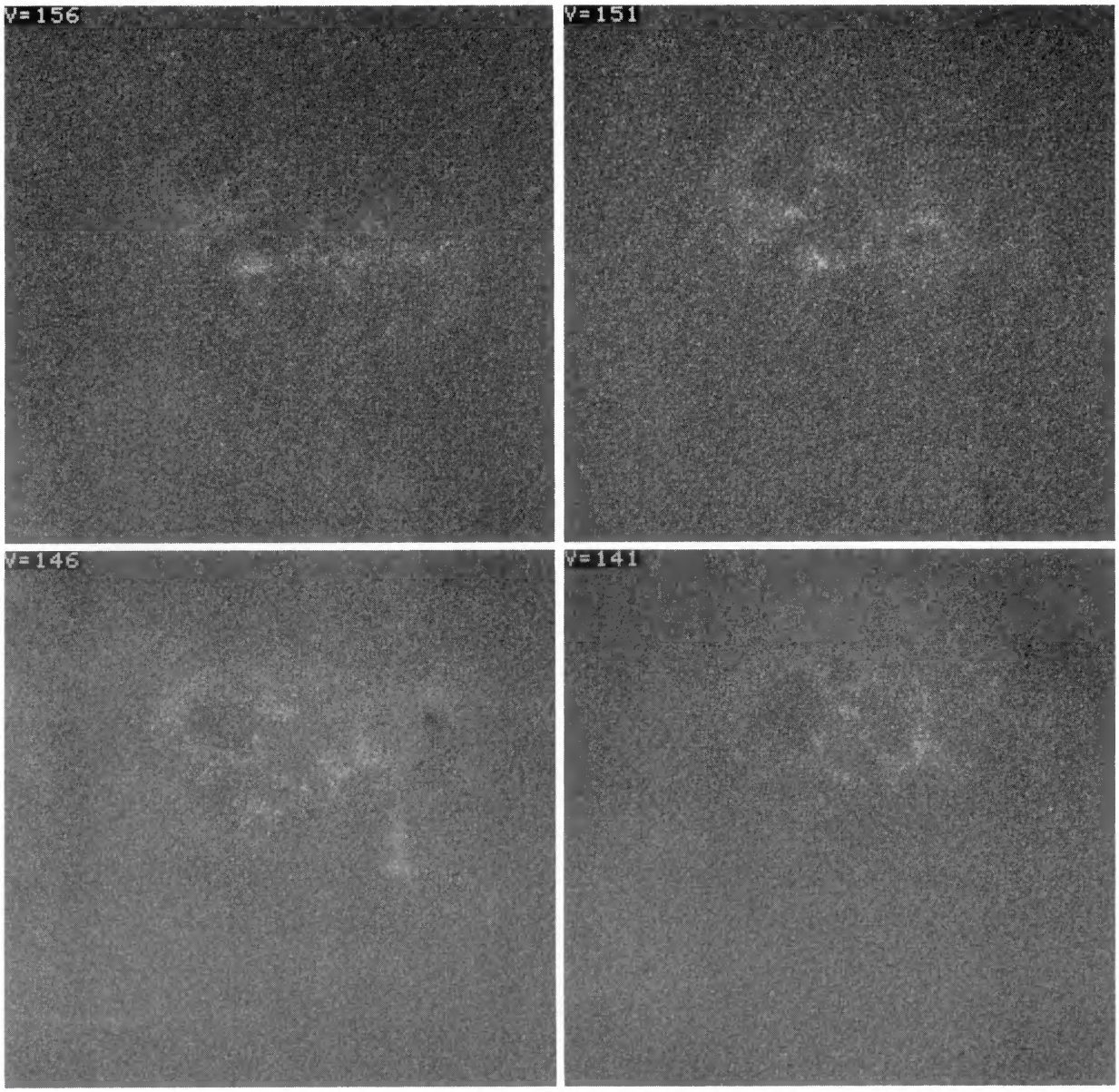

FIG. 1. (continued)

Puche *et al.* (see page 1843)

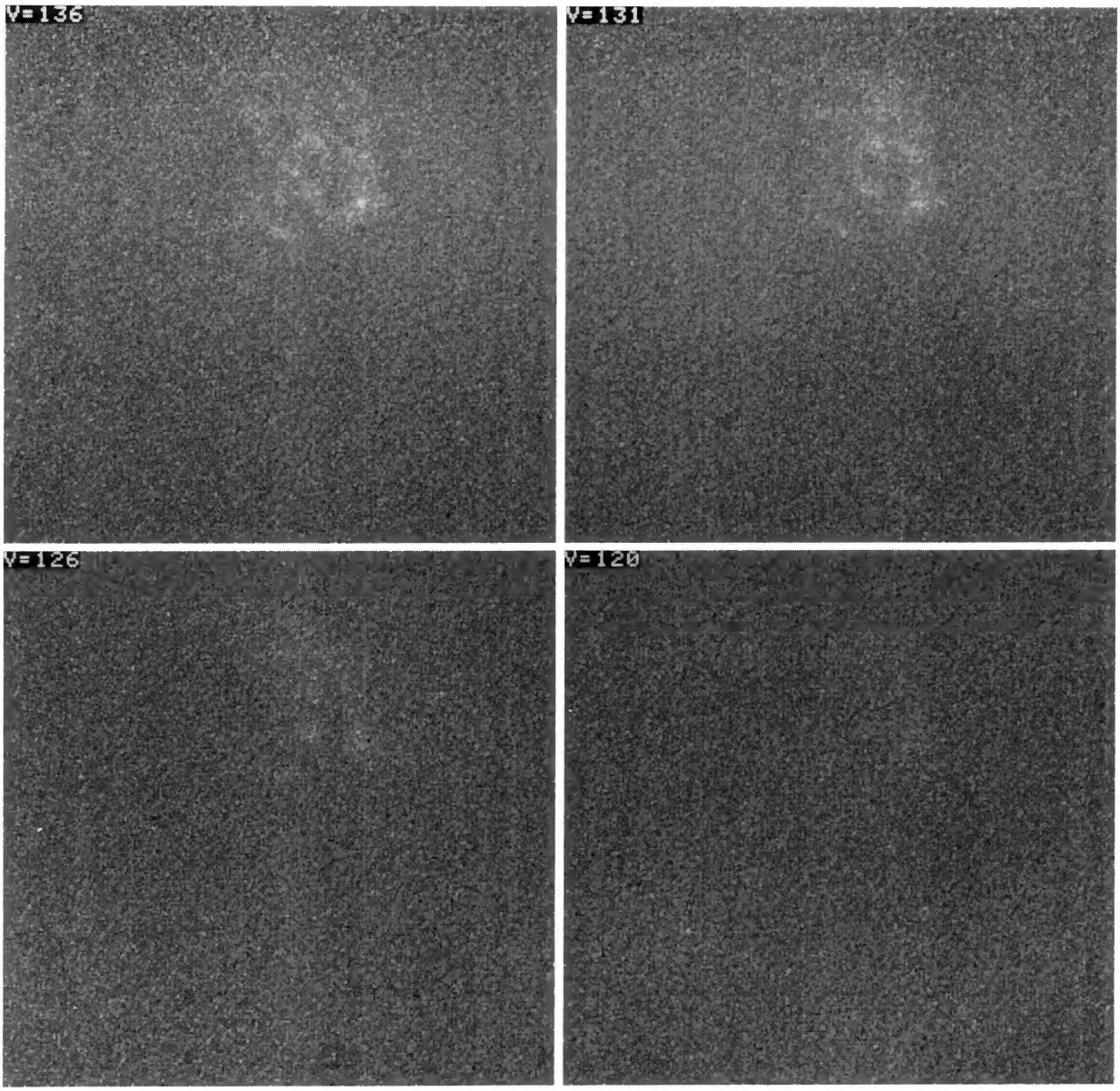

FIG. 1. (continued)

Puche *et al.* (see page 1843)

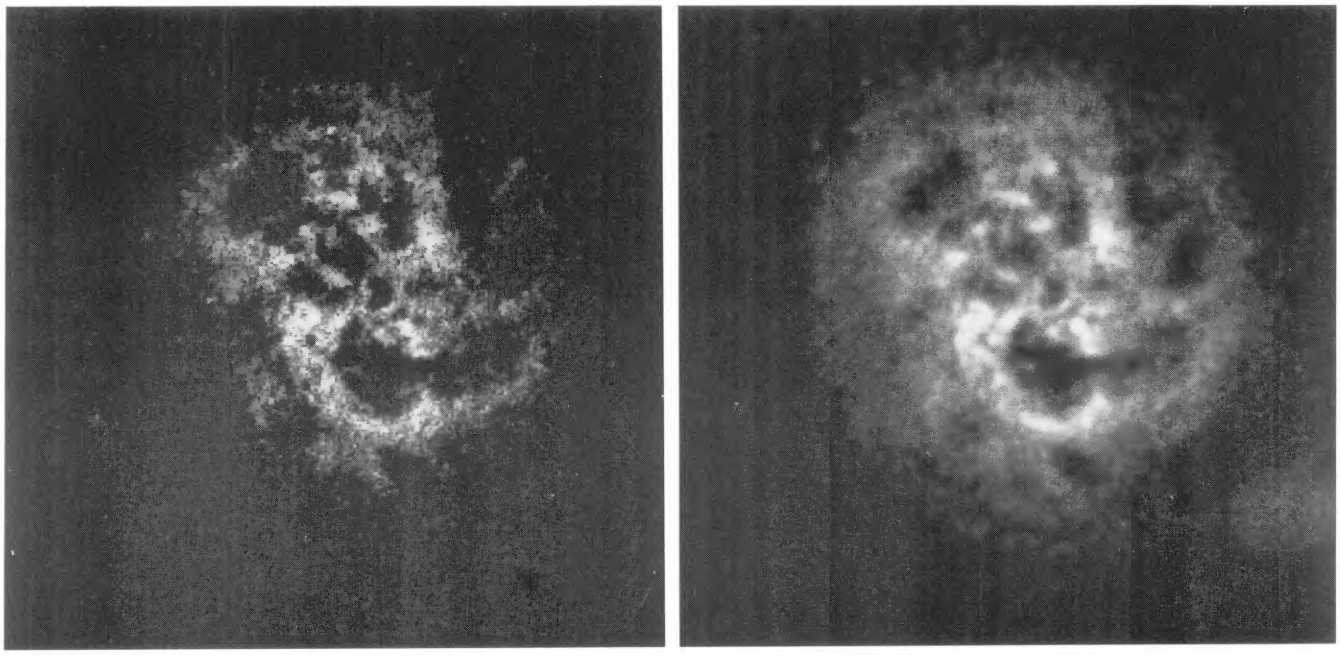

FIG. 3. Total H I maps of Holmberg II obtained from the 4.0″×4.5″ (left) and the 11.0″×10.9″ (right) resolution datacubes.

Puche *et al.* (see page 1843)

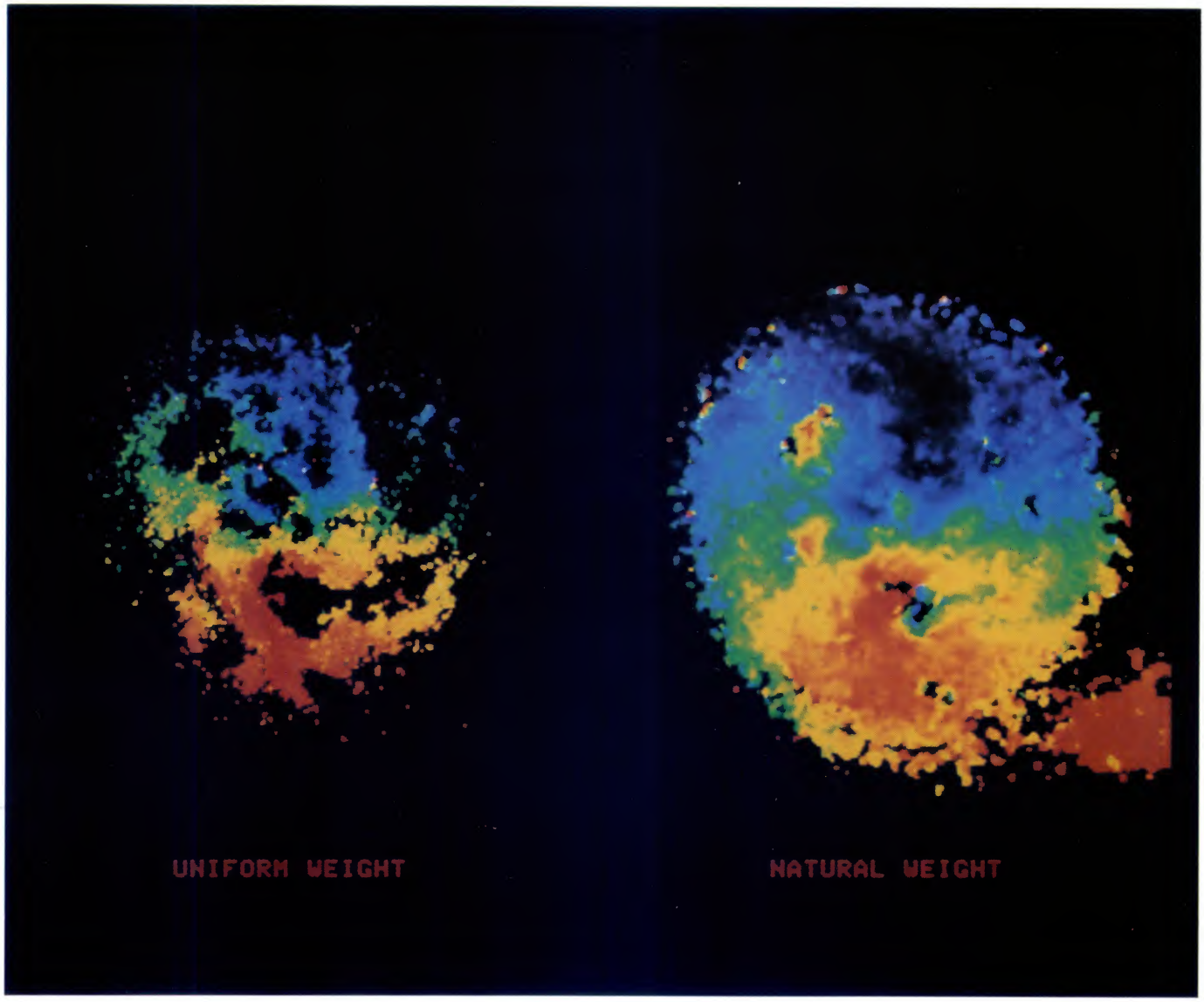

FIG. 4. Isovelocity maps of Holmberg II obtained from the 4.0″ × 4.5″ (left) and the 11.0″ × 10.9″ (right) resolution datacubes. The red color indicates the receding side and the blue indicates the approaching side.

Puche *et al.* (see page 1844)

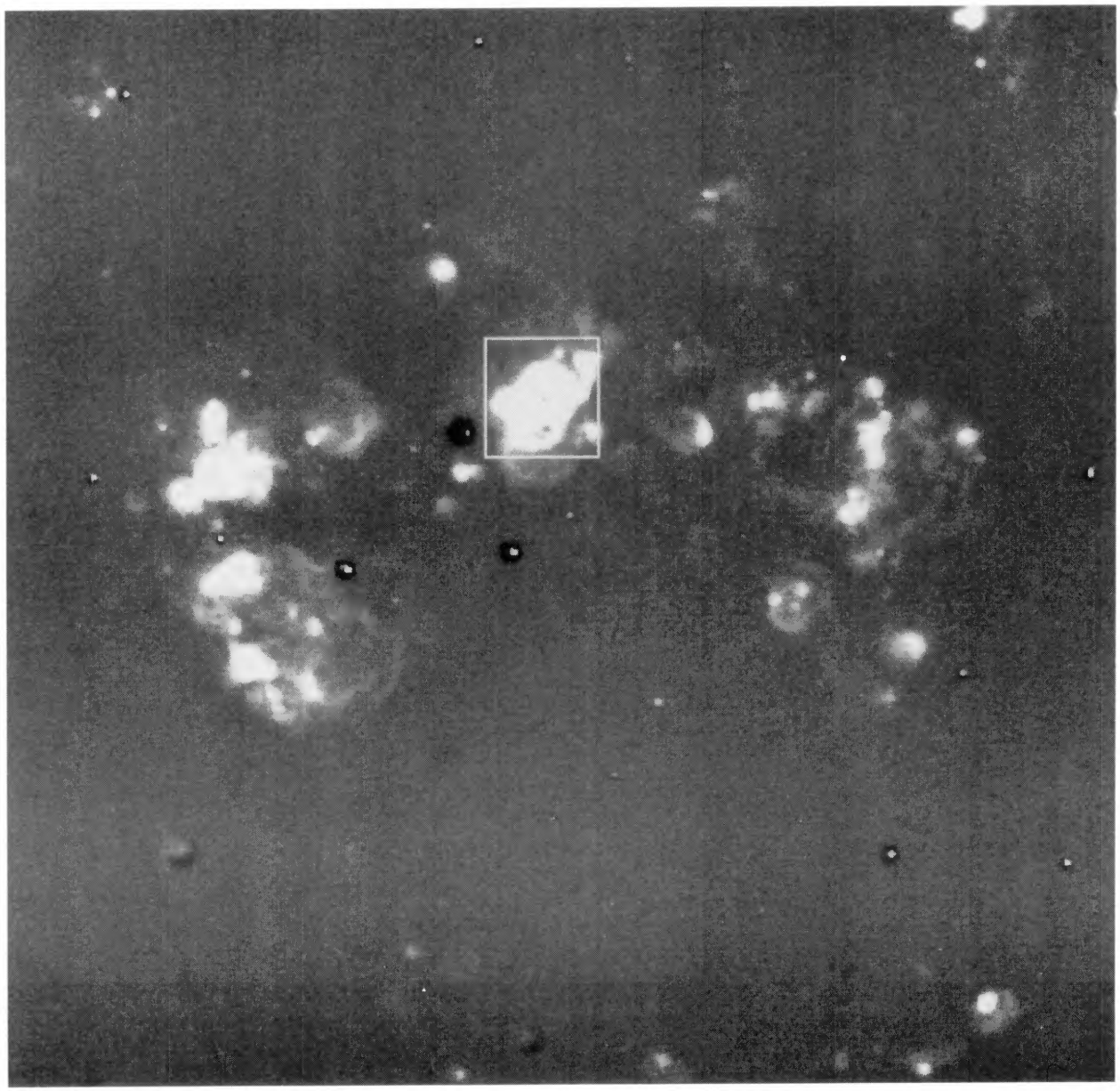

FIG. 8. CFHT Hα image of the central region of HoII [5′×5′ centered at $\alpha(1950) \simeq 8^h14'$, $\delta(1950) \simeq 70°52'$]. The region for which an independent calibration measurement is available is indicated by a box.

Puche *et al.* (see page 1846)

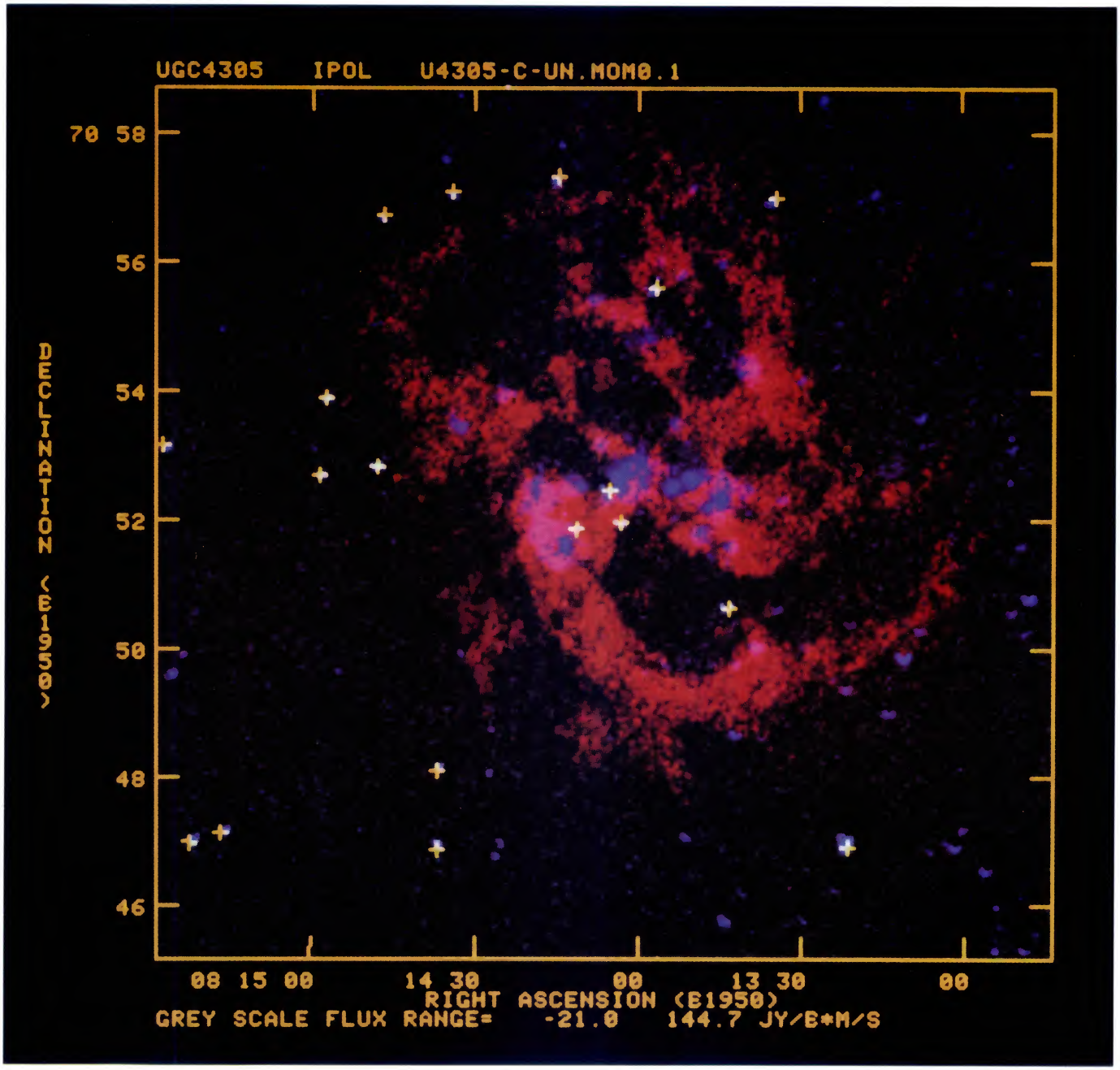

FIG. 21. Hα image (blue) obtained at KPNO overlaid on the H I total surface brightness map at a resolution of 4″ × 4.5″ (red).

Puche *et al.* (see page 1852)

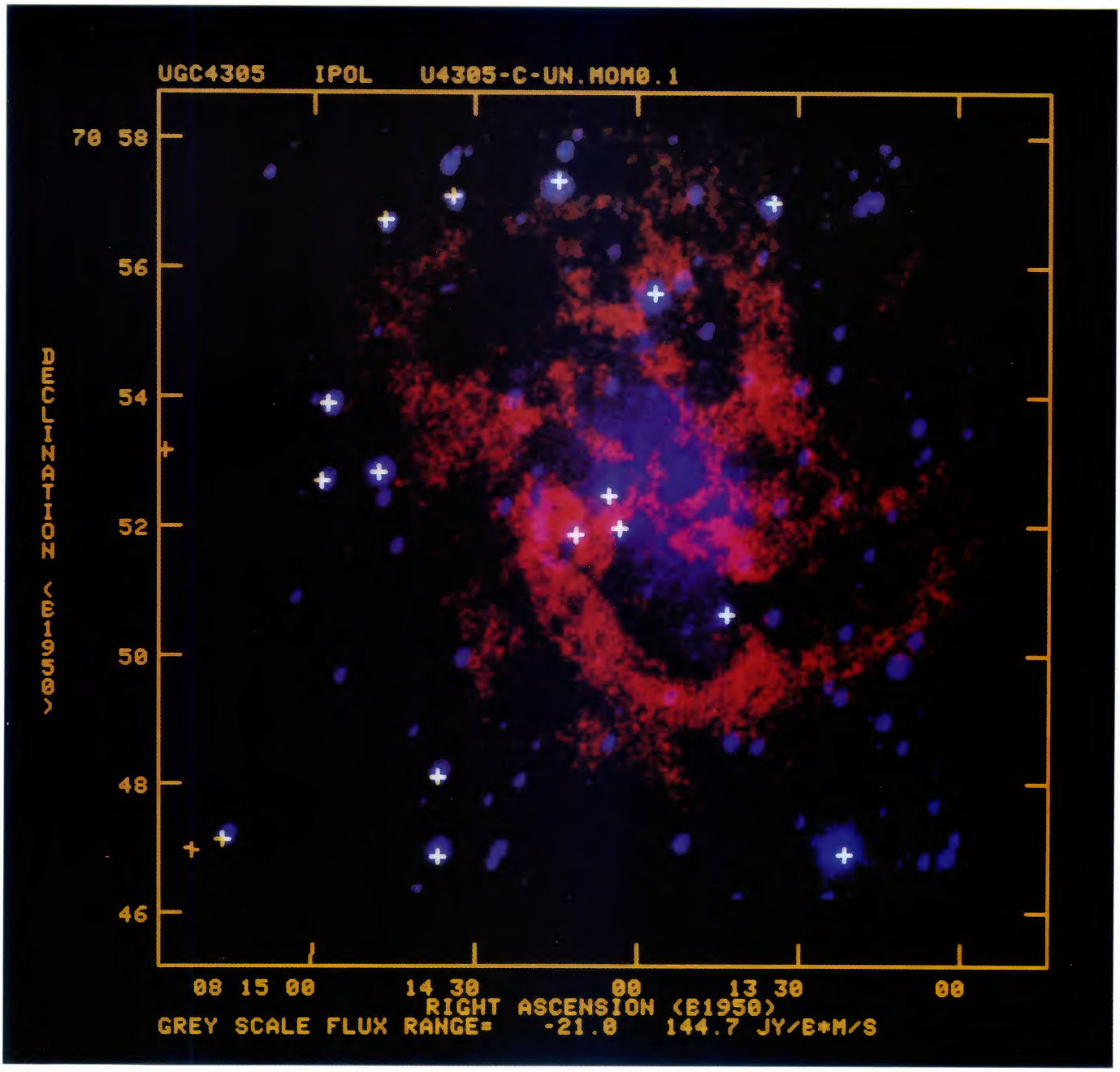

FIG. 22. *R*-band image (blue) from KPNO overlaid on the high resolution integrated H I emission (red).

Puche *et al.* (see page 1852)

THE ASTRONOMICAL JOURNAL

FOUNDED BY B. A. GOULD
1849

VOLUME 103 | June 1992 ~ No. 1637 | NUMBER 6

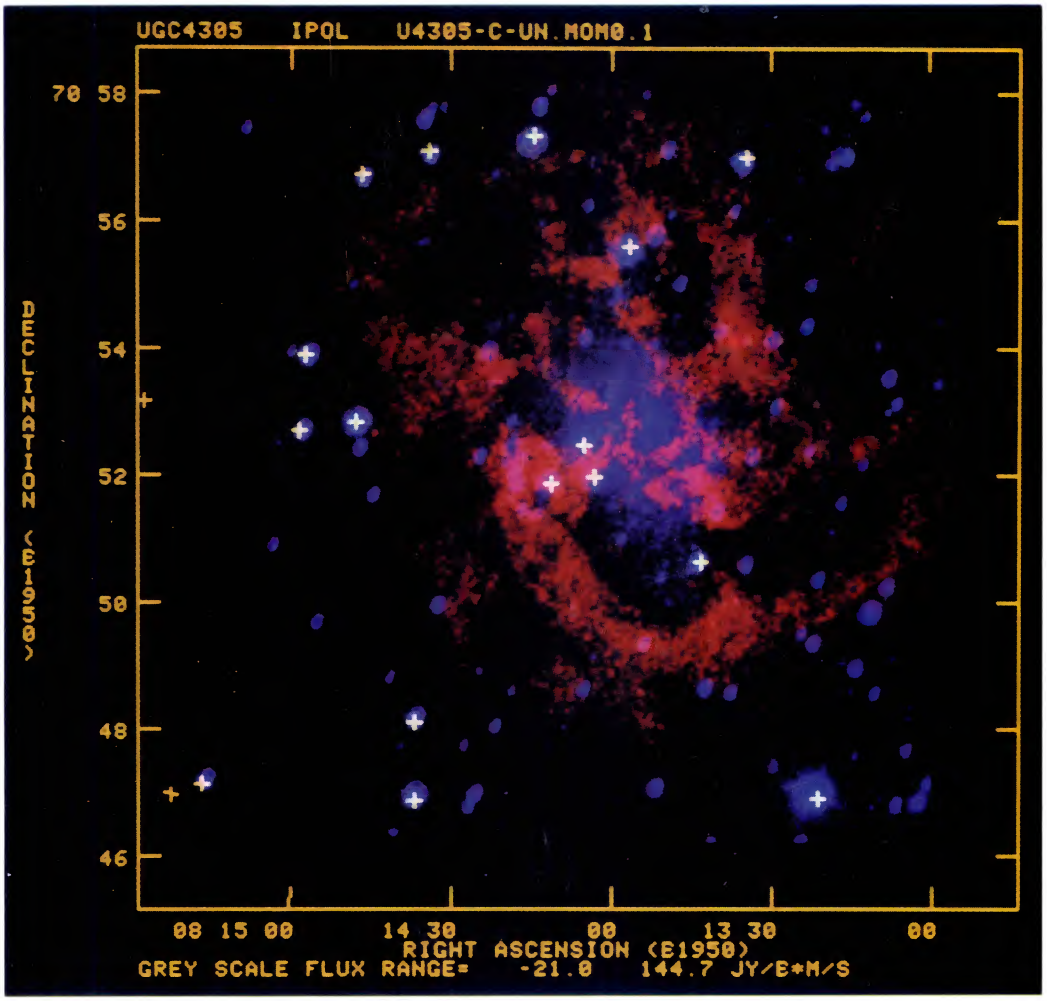

(See Page 1841)

Published for the
AMERICAN ASTRONOMICAL SOCIETY
by the
AMERICAN INSTITUTE OF PHYSICS